Impact of genomic background and developmental state on signaling pathways and response to therapy in glioblastoma patient-derived cells

Artem Berezovsky[1,2¶], Oluwademilade Nuga[1,3¶], Indrani Datta[1], Kimberly Bergman[1], Thais Sabedot[1], Katherine Gurdziel[3,4], Susan Irtenkauf[1], Laura Hasselbach[1], Yuling Meng[1], Claudius Mueller[5], Emanuel F. Petricoin III[5], Stephen Brown[6], Neeraja Purandare[4], Sidhesh Aras[2,4], Tom Mikkelsen[7], Laila Poisson[8], Houtan Noushmehr[1], Douglas Ruden[4,9], Ana C. deCarvalho[1,2,3*]

[1]Department of Neurosurgery, Henry Ford Health, Detroit, Michigan, United States of America

[2]Department of Oncology, Wayne State University, Detroit, Michigan, United States of America

[3]Department of Pharmacology, Wayne State University, Detroit, Michigan, United States of America

[4]Institute of Environmental Health Sciences, Wayne State University, Detroit, Michigan, United States of America

[5]Center for Applied Proteomics and Molecular Medicine, George Mason University, Manassas, Virginia, United States of America

[6]Department of Radiation Oncology, Henry Ford Health, Detroit, Michigan, United States of America

[7]Precision Medicine Program, Henry Ford Health, Detroit, Michigan, United States of America

[8]Department of Public Health, Henry Ford Health, Detroit, Michigan, United States of America

[9]Department of Obstetrics and Gynecology, School of Medicine, Wayne State University, Detroit, Michigan, United States of America

[¶] These authors contributed equally to this work.

*Corresponding author

E-mail: adecarv1@hfhs.org (ACD)

Abstract

Glioblastoma (GBM) tumors encompass several subgroups, reflecting diversity in the genomic epigenomic, and transcriptional landscape. Additionally, remarkable intratumoral heterogeneity, a hallmark of glioblastomas, poses significant challenges to the standard of care, comprised of treatment with radiation (RT) and with the DNA-alkylating agent temozolomide (TMZ). In this study, using targeted proteomics we determined the response of a genomically-diverse panel of patient-derived GBM cells to neural stem and differentiation-inducing culture conditions, unveiling complex crosstalk in key oncogenic signaling. Furthermore, we show both common and tumor specific aspects of transcriptional and epigenetic reprograming accompanying differentiation of cancer stem cells (CSCs). We report the relative impact that differentiation and genomic background have on sensitivity and transcriptional response of GBM cells to TMZ and RT. Importantly, we show that the differentiation of GBM cancer stem cells increased sensitivity to temozolomide but not to radiation treatment. Transcriptional response to treatment was largely dependent on p53 status, while treatment-induced p53 activity was also influenced by the differentiation state of wildtype p53 cells. Interferon response was activated in CSC differentiation and in response to TMZ and RT. The modeling of GBM differentiation states in vitro is a powerful tool for optimizing treatments, emphasizing the necessity of evaluating gene expression patterns associated with cellular adaptations.

Introduction

Glioblastoma (GBM), classified as World Health Organization (WHO) Grade 4 IDH-wildtype astrocytoma, remains the most aggressive and prevalent primary brain tumor in adults [1]. Since 2005, standard of care treatment of GBM includes maximal safe surgical resection [2], followed by ionizing radiation therapy (RT) and the brain-penetrant DNA-alkylating agent temozolomide (TMZ) [3]. Surgery alone is not curative [2] and TMZ provides a modest significant increase in median overall survival in patients with newly diagnosed GBMs when combined with RT compared to RT alone [4]. TMZ sensitivity in newly diagnosed GBMs is modulated by the expression of DNA repair protein, O-6-methylguanine-DNA methyltransferase (MGMT). The silencing of MGMT through promoter hypermethylation is a predictive marker of TMZ sensitivity for newly diagnosed GBMs [5], while MGMT expression is also regulated by DNA methylation independent mechanisms [6, 7]. In addition to *MGMT* promoter methylation, Isocitrate dehydrogenase 1 (*IDH1/2)* mutation and Glioma-CpG island methylator hypomethylation signature (G-CIMP) status are the only other known molecular prognostic markers in GBM patients [8-10]. Considering that more than 70% of GBM patients have actionable targets with existing therapeutic agents [11], clinical trials employing these agents, primarily multi-kinase inhibitors in mono- or combination therapy, have not demonstrated sufficient efficacy in improving overall and progression-free survival [12].

Intra-tumoral heterogeneity (ITH) is a key factor contributing to the GBM resistance to treatment and indeed its high rate of recurrence. Genomically-defined subclonal populations presenting differential sensitivity to pharmacological agents arise after treatment in recurrent GBMs [13]. Another contributor to ITH is oncogene amplification in extrachromosomal DNA (ecDNA), as we previously reported cases of low frequency ecDNA in newly diagnosed GBM exhibiting a notable increase in prevalence at recurrence following treatment [14]. Non-genetic factors also contribute to ITH, such as the high degree of plasticity of GBM cells, reflected in the

ability to transition in a continuum of cell states analogous to neural development, from neural stem/progenitor-like to differentiated astrocyte-like cells, as shown by bulk tumor RNAseq deconvolution and single cell RNAseq analyses [15]. ITH involves dynamic shifts in subclonal composition in response to treatment and to changes in the microenvironment in GBM [16, 17]. Thus, it is important to consider ITH when designing preclinical studies to test optimization of treatment efficacy for GBMs. Ultimately, the diversity in genomic and epigenomic drivers among GBM patients, along with the additional variability associated with dynamic ITH, converge on the deregulation of key oncogenic signaling involving receptor tyrosine kinases (RTK), phosphoinositide 3-kinases (PI3K)/AKT/ mammalian target of rapamycin (mTOR) and mitogen-activated protein kinases (MAPK) pathways; 90% of GBM patients have alterations in either the RTK, PI3K, or MAPK pathway [18]. Cross-activation of MAPK by PI3K signaling in immortalized astrocytes results in increased cell growth and migration [19] and MEK inhibitor-resistant GBM cells are sensitized by combination therapy with a dual PI3K/mTOR inhibitor [20]. Overall convergent signaling nodes of both PI3K and MAP foster aberrant cell growth, proliferation, survival, and resistance to therapeutic interventions [21].

Cancer stem cells (CSCs), a population of stem like cells that maintains tumor heterogeneity through modulation of developmental cellular state [22], has been applied to the development of GBM patient-derived models for pre-clinical studies. An established strategy to select GBM CSC from surgical samples consists of culturing dissociated tumor samples in selective serum-free media, originally formulated for the isolation of mouse neural progenitor cells, resulting in “neurosphere” 3D cultures [23, 24]. In this context, CSCs are defined by their long-term self-renewal in culture and their ability to differentiate and recapitulate the original tumor upon orthotopic implantation in immunocompromised rodents [25, 26]. In recent years, the use of GBM neurosphere cultures have been extensively validated as a renewable source of patient-derived neoplastic cells with remarkable genomic fidelity to the original tumor [14, 27, 28]. These neurosphere/CSC cultures are amenable to in vitro biology and experimental

therapeutics studies [29], and suitable for in vivo xenograft validation in immunocompromised rodents. To enhance the translational applicability of in vitro investigations aimed at optimization of treatment efficacy in GBMs, it is imperative to consider the influence of patient genomic diversity and intratumoral phenotypic variability. The objective of this study is to investigate the contributions of somatic genomic alterations in conjunction with the neoplastic cell developmental state modulating key signaling pathways and response to TMZ and RT in GBMs. Employing targeted proteomics, we accessed changes in signaling between GBM CSC cultures subjected to astrocytic differentiation, growth factor withdrawal, or conventional cell culture in 10% fetal bovine serum (FBS), using a genomically-diverse panel of CSCs derived from newly diagnosed GBM patients [14, 30, 31]. Transcriptional remodeling in response to astrocytic differentiation of CSCs reveled common traits among the cell lines, such as maintenance of the expression of a subset of stemness genes, decrease in cholesterol biosynthesis, and increase in ECM production. Other pathways activated upon differentiation were cell specific, such as activation of the interferon (IFN) response. We show that differentiation of CSCs increases resistance to temozolomide but not to radiation, and that transcriptional responses to TMZ and RT are largely controlled by p53, but also include the expression of IFN response genes and epithelial mesenchymal transition. We show that modeling the differentiation of CSCs in vitro provides a powerful platform to uncover the interaction of genomic landscape, cell state and signaling, and response to treatment.

Results

Alterations in key cell signaling pathways in glioblastoma cancer stem cells in response to astrocytic differentiation, growth factor withdrawal and traditional 10% FBS media.

CSCs derived from 8 newly diagnosed GBM patients, representing the main genomic drivers were selected for this study (Fig 1A). These CSC lines meet the requirement of the two defining stemness criteria: long term self-renewal and orthotopic tumor formation in immunocompromised mice [14, 30, 31]. FBS, a supplement supporting the culture of a variety of mammalian cells, contains hormones, growth factors, cell attachment factors and other nutrients [32]. Media supplemented with 10% FBS had been widely employed to propagate glioma cells in culture, prior to seminal data demonstrating artificial genetic drift occurring from serial passaging under these conditions [33]. In contrast, 1-2% FBS added to defined media has been successfully used to differentiate hiPSC-derived neural stem cells into astrocytic lineage [34, 35]. To model more differentiated phenotype in culture, CSCs growing in 3D cultures in defined neurosphere media supplemented with, 20 ng/ml each epidermal (EGF) and basic fibroblast (bFGF) growth factors (NMGF), were differentiated into an astrocytic phenotype in NMGF supplemented with 2% FBS for 14 days, which we call here “serum differentiated cells” (SDC). For comparison, we tested two additional growth conditions: growth factor-depleted neurosphere media (NM), or media supplemented with 10% FBS (10% FBS) (Fig 1B). After 2 weeks in culture, cell lysates were obtained and analyzed by Reverse Phase Protein Arrays (RPPA) in triplicates, as described [36, 37]. The levels of 66 proteins or post-translational modifications (PTM) in the cell lysates were quantified (S1 Table). Pairwise comparisons between NMGF CSC culture and either NM or 2% FBS/SDC for the 8 cell lines did not show a global shift in the levels of protein/PTMs levels (S1_Fig), but important patterns of alteration in specific signaling were observed. Phosphorylation levels of Ser-residues in receptor-dependent r-Smad1/5/8, which are primarily activated by BMP ligand signaling, were notably upregulated in SDCs in relation to CSCs in all 8 GBM models (Fig 2A). Consistent with BMP ligands being present in FBS [38], increased levels of p-Smad1/5/8 were also observed in 10% FBS cultures for all models (S1 Table). The activation of PI3K downstream of RTK signaling leads to the accumulation of lipid secondary messenger phosphatidylinositol (3,4,5)-trisphosphate (PIP3),

which in turn promotes pyruvate dehydrogenase kinase 1 (PDK1) activation of AKT via phosphorylation of T308 residue. mTORC2 further phosphorylates AKT on S473 to fully activate the kinase [39]. The tumor suppressor phosphatase and tensin homolog (PTEN) opposes AKT activation by dephosphorylation of PIP3. PTEN function is frequently lost in GBMs through gene deletion and mutations, as seen in 7/8 GBM tumors represented in this study (Fig 1A). AKT phosphorylation at both Y308 and S473 was suppressed in the absence of growth factors (NM) for all lines, except for HF2927, which carries ligand independent EGFRvIII amplification. In 2% FBS (SDCs), AKT phosphorylation was suppressed for HF2587, HF3035 and HF3077, and upregulated or unchanged in the remaining models (Fig 2A). In response to growth factor withdrawal, phosphorylation levels of S6 ribosomal proteins (RBS6), downstream of mTORC1, were decreased while phospho-ERK increased for most CSC lines (Fig 2A). Phospho-EGFR (Y1173 and Y1068) was increased in response to growth factor withdrawal exclusively in the EGFRvIII line HF2927 (Fig 2A). Expression of MET proto-oncogene, receptor tyrosine kinase (cMET) was observed for all CSCs (S1 Table), but in the absence of MET ligand (hepatocyte growth factor) in the media, only HF2927 and HF3016 presented modest levels of MET activation, which was suppressed in 2% FBS (Fig 2A).

Fig 1. Glioblastoma patient-derived models and experimental design. A) Clinical and molecular data associated with the GBM patient-derived models. RT, radiation therapy; TMZ, temozolomide; Rx1, first-line therapy; TTP, time to progression; OS, overall survival; U, unmethylated; M, methylated MGMT promoter. Red outline denotes extrachromosomal (ecDNA) amplification. **B)** Schematic depicting neurosphere culture in NMGF media for selection and amplification of cancer stem cells (CSCs) from surgical specimens, followed by 2 weeks incubation in altered conditions: withdrawal of growth factors (NM), and addition of 2% and 10% FBS. For the purposes of this study, serum-differentiated cells (SDC) are those cultured in 2% FBS. The effect of the different culture conditions on cell signaling were compared by RPPA. **C)** The sensitivity of CSC and SDC for a subset of the models to single dose radiation (RT) or 5-day TMZ was measured. Transcriptional and epigenomic reprograming in SDC vs CSC, and in response to treatment were evaluated by bulk RNAseq and 450k DNA methylation array.

Fig 2. Targeted proteomics reveals common and cell specific alterations in key signaling CSCs in response to differentiation and identifies interdependencies in activation of key signaling mediators. A) Heatmap depicting log2FC relative to NMGF (CSC) for the top 5% most variable proteins/PTM. Each value represents mean log2FC for n=3 RPPA measurements/group. proteins/PTMs which were not detected under all three culture conditions were filtered out for each model (grey cells). **B)** Heatmap of Spearman correlation coefficient

values comparing phosphorylation levels in key cell signaling mediators in 8 patient derived GBM models grown in 4 media conditions in triplicates.

We used this unique targeted proteomics dataset, integrating various genomic backgrounds and culture conditions, to investigate the signaling networks in glioblastoma. The Spearman correlation of key proteins and post-translational modifications levels in all 96 samples (8 GBM lines in 4 media conditions in triplicate) was calculated and displayed in the heatmap (Fig 2B). Glycogen synthase kinase-3 (GSK3)α/β is a multifunctional kinase frequently inhibited by phosphorylation downstream of PI3K/AKT, mTORC1 or MAPK signaling. Here we observed that phosphorylation of GSK3α/β at S21/S9 was strongly correlated with AKT activation (Fig 2B). While mTOR complex 1 (mTORC1) is activated by AKT [40], in this dataset AKT activation did not correlate with markers of mTORC1 activation, such as mTOR phosphorylation at the C-terminus S2448 residue [41], p70 ribosomal protein S6 kinase 1 (S6K) phosphorylation at T412, or phosphorylation of RBS6 [42] (Fig 2B). On the other hand, phosphorylation of AMP-activated protein kinase (AMPK) subunit β1 at S108 was highly correlated with mTORC1 activation (Fig 2B). AMPK αβ heterotrimeric complex is activated in response to low oxygen, low nutrients, and DNA damage, playing important roles in cancer [42]. AMPK is inactivated by AKT phosphorylation of AMPKα1 at S485 residue, while phosphorylation at AMPKβ1 S108 sensitizes AMPK to agonists [43], having a function in pro-survival pathways [44]. Src activity is inhibited by phosphorylation of Y527 by C-terminal Src kinase (CSK) and regulated by dephosphorylation by protein tyrosine phosphatases (PTPs), leading to conformational change and autophosphorylation of Y416 [45]. Levels of inhibitory Src phospho-Y527 were elevated in HF2354, HF2587, HF3016 and HF3077 relative to other CSC lines while the levels of Src phospho-Y416 were less variable among CSC lines and media conditions (S1 Table) and positively correlated with Src phospho-Y527 (r=0.705, CI: 0.584 to 0.796), but not with phospho-Stat3 (S727), a canonical downstream signal transducer (Spearman correlation, r=0.302, CI: 0.1026 to 0.4788) (Fig 2B). Phospho-Stat3 was positively

correlated with mTORK1 (phospho-mTOR, phospho-SK6) and MAPK (phospho-RSK) signaling (Fig 2B). Signaling through insulin like growth factor 1 receptor (IGF1R) and insulin receptor (IR) promotes cancer cell proliferation, survival, and treatment resistance in diverse malignancies. Upon ligand binding, IGF1R homodimer or IGF1R/IR heterodimer receptors recruit insulin receptor substrate (IRS) adaptor protein to transduce downstream signaling through binding of src-homology-2 (SH2) proteins, such as p85 to activate PI3K and Grb2 to activate ERK [46]. All four media conditions tested here contain insulin at a final concentration of 50 µg/ml (N2 supplement), which has been shown to activate IGF1R, although at a lower rate than the canonical ligand IGF2 [47], while the FBS supplemented media contain additional insulin and IGF1/2 ligands [32]. Consistently, activation of IGF1R (phospho-Y1135/Y1136) / IR (phospho-Y1150/Y1151) presented little variation among GBM lines and culture conditions (S1 Table). mTORC1 phosphorylates IRS1 at S616 residue leading to the adaptor turnover [48], but p-IRS1 did not correlate with mTORC1 activation. Instead, a strong correlation of p-IRS1 with inactivating phosphorylation of forkhead box protein O1 (FOXO1/FKHR) on S256, which is attributed to AKT [49], was observed (Fig 2B).

Z-scores were calculated for each protein/PTM based on its distribution across all 8 models and 4 media conditions, and cumulative z-scores were determined for key signaling pathways and cellular functions (S1 Table). Interestingly, we observed a remarkable pattern of inhibition for key signaling pathway and functions in 10% FBS, in contrast with 2% FBS (SDC) cultures (Fig 3A), further corroborating the inadequacy of culturing GBM cells in 10% FBS [33, 50]. Receptor tyrosine kinase activation ("RTK") index, based on the levels of Tyr phosphorylation corresponding to activation of 11 RTKs (S1 Table), decreased in 2% FBS (SDCs) relative to CSCs in HF2927 and HF3016, the only 2 models harboring EGFR amplification on extrachromosomal DNA (ecDNA) [14], and increased in the remaining 6 GBM models (Fig 3A). The levels of EGFR were 10-fold higher for HF2927 CSCs, which also carries the EGFRvIII variant (Fig 1A), relative to HF3016, while the levels of phospho-EGFR at carboxy-

terminal Y1068 and Y1173 residues were comparable for these 2 CSC lines (Fig 3A). Interestingly, EGF withdrawal for 2 weeks (NM) led to a 4-fold increase in the levels of EGFR activation in HF2927 (S1 Table, Fig 2A), suggesting an inhibitory effect of long-term exposure to EGF ligand on EGFRvIII. RTK activation correlated with downstream RTK signaling pathway ("TK_Signaling"), which includes both MAPK and PI3K/Akt/mTOR ("PI3K") pathways (Fig 3A). As part of RTK signaling convergence, SHC Adaptor Protein 1 (SHC1) binds to phosphorylated EGFR Y1173, which is further phosphorylated on Y239 and Y317 resulting in recruitment of Grb2 and downstream activation of MAPK and PI3K/AKT pathways [46]. Phospho-Shc1 (Y317) was only observed for HF2927 and HF3016 CSCs, and in both cases upregulated upon growth factor withdrawal (NM) and downregulated in the presence of FBS, following the pattern of EGFR activation (S1 Table, Fig 2A). MAPK signaling activation and cytoskeletal function, consisting of regulation of actin and microtube dynamics (S1 Table), were maintained or increased in SDCs for all models except HF2927 and HF3016 (Fig 3A), analogous to what we observed for the RTK index. The PI3K/AKT/mTOR pathway activation score was low for HF2927 CSCs, relative to the other CSC lines, and remained low in NM and 2% FBS, despite genomic loss of PTEN, EGFRvIII amplification, and high level of EGFR activation (Fig. 2A). PI3K/AKT/mTOR activation index was higher for the other 7 CSCs, maintained in SDCs, and decreased in the absence of growth factors (Fig. 3A).

Fig 3. **Comparative targeted proteomics of CSCs growing in 4 different conditions. A)** Heatmap depicting mean signaling pathway activation for triplicate samples in 4 culture conditions, for CSCs derived from 8 patients with diverse genomic landscape, transcriptional subclass and MGMT promoter methylation. Hierarchical clustering of rows was based on Spearman correlation analysis. **B)** Heatmap for protein/PTM z-scores involved in cell death and survival signaling for 3 models grown in NMGF (CSC), NM and 2% FBS (SDC), in triplicate (boxes in (A)).

Since several of these signaling pathways are involved in cell survival and proliferation, we established a "viability index" measuring the net result from the sum of the level of protein/PTM associated with cell survival and proliferation minus the level of markers associated with programed cell death (S1 Table). We observed that culture conditions did not impact the

viability index uniformly (Fig 3A). Three models, HF2303, HF2927 and HF3016, representing a range of viability index values, each of the 3 transcriptional subclasses, and diverse genomic features, were selected for further characterization. Levels of key signaling components associated with cell death and survival are shown (Fig 3B). High PTEN expression was observed in HF2303, harboring pathogenic p.D92E mutation in the WPD loop [51], corresponding to a high level of phosphorylation at S380 in the carboxy terminal tail, a crucial post-translational modification for blocking proteasomal degradation [52]. High levels of AKT activation observed for HF2303 CSCs were further increased in SDCs, indicating that the p.D92E mutation impairs PTEN ability to inhibit AKT. Conversely, PTEN levels were very low in HF3016, which carries a pathogenic mutation in the P-loop, p.I122S [51], comparable to PTEN-null HF2927 (Fig 3B). Increased levels of phospho-ERK and phospho-JNK were observed for HF2303 and HF2927 in response to growth factor withdrawal (NM). In HF2303, the increase was also observed in SDCs, relative to CSCs. The levels of p53 protein were consistent with the mutation status for these lines (Fig 3B).

CSCs present increased sensitivity to temozolomide but not to radiation compared to isogenic SDCs.

MGMT epigenetic silencing is a clinically used biomarker to predict response to TMZ treatment. HF3016 and HF2303 CSCs were derived from tumors with unmethylated and HF2927 CSC from a tumor with methylated MGMT promoter (Fig. 1A). We confirmed the promoter methylation status for HF2303 and HF2927 cells and did not observe changes in methylation between CSC and SDCs (S2_Fig). Accordingly, HF2927 cells presented the lowest level of MGMT protein. Despite both having unmethylated promoter status, MGMT levels were 2.5-fold higher for HF3016 relative to HF2303 (Fig. 4A, S1 Table). MGMT protein level was stable in all three culture conditions for HF2303, while it was significantly decreased in SDCs relative to CSCs for HF2927 and HF3016 (Fig 2C). We observed that MGMT expression pattern

in the two models with unmethylated promoter, HF3016 and HF2303 (Fig 4A), was highly correlated (Spearman r =0.823; 95% CI: 0.6213 to 0.9228) with the levels of activated nuclear factor-kappa B (NF-κB) p65 (phospho-S536) (Fig 3B, S1 Table). Remarkably, the correlation between activated NF-κB and MGMT levels was significant for all GBM cells, regardless of promoter methylation status, but stronger for unmethylated MGMT samples (Fig 4B). To investigate to what extent the developmental state affected the sensitivity of GBM cells to genotoxic treatments, CSC and SDCs from HF2303, HF2927 and HF3016 were treated with TMZ and radiation (RT) (Fig 1C). These models represent diverse molecular characteristics known to modulate response to DNA-damaging agents, such as TP53 status and MGMT promoter methylation. First, we compared cell proliferation rates between 3D CSC and 2D SDC cultures. SDCs proliferated at a higher rate than CSCs for HF3016 only, while no significant difference was observed for the other two lines (Fig 5A). Cells were then treated for 4 days with doses ranging from 0 (DMSO) to 400 μM TMZ, in quintuplicates. To compensate for possible binding of TMZ by proteins in FBS, even at the low concentration used, the serum-free neurosphere media was supplemented with bovine serum albumin (1%) [53]. Dose-response curves were generated by non-linear fitting, and IC50 and area above the curve (AAC) were calculated. Differentiation of CSCs into SDCs increased resistance to TMZ for all three lines (Fig 5B), despite decreased baseline MGMT protein observed for HF2927 and HF3016 SDCs (Fig 4A). HF2927 cells were more sensitive to TMZ in comparison with the other two cell lines (Fig 5B), as expected based on MGMT promoter methylation and expression (Fig 4A).

Fig 4. The impact of culture conditions on MGMT protein expression is cell line specific and correlates with NFkB activation. A) MGMT protein levels measure by RPPA for the same samples described in (B). P-values for 1-way ANOVA and post-hoc TukeyHSD test for comparison of the effect of culture conditions on MGMT protein expression are shown. **B)** Correlation of the levels of MGMT and phospho-NFkB (S536), for all 8 GBM models and culture conditions (left panel) and for the 4 models presenting unmethylated MGMT promoter (right panel). Spearman r and 95% CI are shown.

Fig 5. GBM CSCs are more sensitive to temozolomide than SDCs. A) To compare cell proliferation rates, CSCs and SDCs for each line were plated in the respective media in 96-well

assay plates (1,000 cells/well) and cell viability was measured over 11 days in culture (n=5). Graphs represent mean (SE). The calculated doubling-times (DT, days) are shown, pairwise comparison between CSC and SDC values were significant for HF3016 only (*) $p<0.01$. **B)** Cells were plated in 96-well assay plates (2,000/plate) and treated for 5 days with the indicated doses of temozolomide, or equivalent DMSO control. Dose-response curves, the calculated IC50 concentrations with confidence interval (CI), and area above the curve (AAC) expressed as a fraction of total area with SE are shown. For each of the GBM patients, CSCs were significantly more sensitive to TMZ relative to SDCs, as shown by IC50 and AAC ratios, and p-values for dose-response curve comparison (F-test).

We then compared the sensitivity of CSCs and SDCs to clinically relevant doses of ionizing radiation (RT). Isogenic populations of CSCs and SDCs were exposed to 2 Gy and 4 Gy ionizing radiation doses, surviving fractions (SF2 and SF4) relative to control treatment were determined 5 days later, as previously described [54]. (Fig 6A). Sensitivity to RT was variable among these models, as a high degree of resistance was observed for HF2303 cells relative to both HF3016 and HF2927; HF2927 was the most sensitive (Fig 6A). On the other hand, no significant difference in sensitivity to RT between CSCs and SDCs were observed for the three models examined (Fig 6A). To evaluate the long-term effect of radiation, we compared the tumorigenic potential of control and RT treated CSCs. Cells expressing luciferase were implanted intracranially in nude mice immediately after radiation (4 Gy), or mock radiation (control). Tumor growth was monitored by bioluminescence imaging and surveillance of symptoms associated with tumor burden. The three irradiated CSC lines exhibited a delay in tumor growth relative to controls, assessed by symptom-free survival, with all mice eventually developing tumors, demonstrating that cells surviving 4 Gy RT dose were tumorigenic. The degree of difference in survival curves (Log rank p-values) ranked according to the in vitro sensitivity of each cell line to RT. Specifically, HF2303 displayed the highest resistance to RT in vitro and exhibited the least significant difference in the survival curves. On the other hand, the HF2927 cells, which were the most sensitive to RT in vitro, displayed the lowest p-value in the curve comparison (Fig 6B,C).

Fig 6. Response of glioblastoma CSCs and SDCs to ionizing radiation. **A)** CSC and SDC received a single radiation dose (2Gy or 4Gy) or mock radiation (control), and cell viability was measured 5 days later (n=3-4). No significant difference in sensitivity to RT between CSC and

SDCs was observed for any of the lines (Holm-Sidak multiple comparisons test with adj p-value<0.05 threshold). The SF values among the 3 cell lines (CSC and SDC combined) were compared by one-way ANOVA, followed by Tukey's multiple comparisons tests, adj p value<0.0001(***), <0.05 (*). **B)** Irradiated and control CSCs were implanted intracranially immediately after treatment, 3x10^5 cells/mouse (n=6-8/group). Symptom-free survival for the orthotopic PDX is shown in Kaplan-Meier curves, compared by log-rank test. **C)** Longitudinal live bioluminescense images for representative PDX in (B).

Transcriptional reprogramming in response to CSC differentiation

To determine how differentiation state impacts transcriptional reprogramming in response to TMZ and RT, we selected the most resistant (HF2303) and the most sensitive (HF2927) models. We first determined the pattern of global transcriptome changes after differentiation of CSCs into SDCs from bulk RNAseq data. To identify differentially expressed genes between the two differentiation states, we employed the non-parametric NOISeq R package, and subsequently performed pathway enrichment analysis, as detailed in the Materials and Methods section. Patterns of transcriptome reprogramming in response to differentiation that were common to both HF2927 and HF2303 models included downregulation of genes involved in cholesterol biosynthesis and upregulation of genes associated with ECM components and organization, including collagen type IV alpha 6 chain (*COL4A6*), a target of SOX2 transcriptional regulation [55] (Fig 7). FBS (2%) in SDC media provides both attachment factors stimulating ECM production, and cholesterol, which is typically transported from the microenvironment by glioblastoma cells [56], but must be synthetized by CSCs cultured in serum-free media. The expression of several transcription factors associated with stemness and pluripotency, such as *SOX2, SALL2 and POU5F1* (Oct3/4), was not altered upon differentiation of HF2303 and HF2927 CSCs into SDCs (A,B in S2 Table), consistent with our previous findings that the role of SOX2 is not restricted to cancer stem cells in glioblastoma, but extends to maintaining plasticity in differentiated cancer cells [31]. On the other hand, other neural progenitor and stemness markers expressed in CSCs were down regulated upon differentiation:

oligodendrocyte transcription factor 1 (*OLIG1*) in both lines; delta like canonical Notch ligand 3 (*DLL3*), integrin subunit alpha 6 (I*TGA6*), ETS variant transcription factor 4 (*ETV4*) in HF2927; fatty acid binding protein 7 (*FABP7*), oligodendrocyte transcription factor 2 (*OLIG2*) and ELOVL fatty acid elongase 2 (*ELOVL2*) [57] in HF2303 (Fig 7). Other signaling pathways and cellular processes enriched in CSCs were cell line specific. It has been proposed that CSCs, from glioblastoma and other cancers, tend to rely more on oxidative phosphorylation (OXPHOS) then the more differentiated cancer cells [58], here we observed that OXPHOS gene expression signature was enriched in HF2303 CSCs but not HF2927 CSCs (Fig 7). Interestingly, reserve respiratory capacity was higher in untreated HF2303 relative to HF2927 cells, and higher in SDC compared to CSCs (S3_Fig). Replication-dependent histones were highly enriched in HF2303 CSCs, in the absence of enrichment in cell proliferation markers (Fig 7, A in S2 Table), as previously observed for embryonic and induced pluripotent stem cells [59]. Several nuclear pseudogenes with sequence similarity to mitochondrially encoded 16S rRNA (e.g. *MTRNR2L1, MTRNR2L3*), enriched in HF2303 CSCs (A in S2 Table) are predicted to encode humanin-like peptides and to be involved in negative regulation of the execution phase of apoptosis [60] (Fig 7). IL2-STAT5 signaling was specifically upregulated in HF2927 CSC in relation to SDC (Fig 7), in agreement with levels of pSTAT5_Y694 being elevated in HF2927 CSC (4.697 $\pm$ 0.98), while undetectable in HF2927 SDCs and HF2303 cells (B in S1 Table).

Fig 7. Transcriptional reprograming in glioblastoma cells in response to CSC differentiation. HF2927 and HF2303 CSC were grown in regular neurosphere media or in SDC cultures for 2 weeks. Total RNA from triplicate samples for each group was sequenced analyzed and DEG between CSC and SDC determined for each line. Total number of upregulated and downregulated protein coding (PC) and non-coding (NC) genes. Select genes from each list are shown. Metascape gene-set enrichment tests were adjusted for multiple comparisons, pathways with q-value < 0.05 are shown. The 43 genes upregulated in CSCs and the 25 genes upregulated in SDCs for both cell lines, along with enriched cellular processes are shown in the grey boxes.

The 24 genes commonly upregulated in SDCs for both lines were enriched in ECM components (Fig 7), which is consistent with production of ECM by astrocytes and differentiated GBM cells [61]. Small nucleolar RNAs were also upregulated upon differentiation of both

HF2303 and HF2927 (S2 Table) (Fig 7), including SNORD116 cluster, shown to have non-canonical functions in the differentiation, survival, and proliferation of neuronal cells [62]. Other transcriptional reprogramming in SDCs were tumor specific. Interferon (IFN) and interleukin signaling were specifically upregulated in HF2303 SDCs (Fig 7). Indeed 29 genes associated with IFN response pathways were upregulated in HF2303 SDCs (Table 1), including members of the 49-gene interferon-related DNA damage resistance signature (IRDS) [63]. Differentiation of CSCs into SDCs resulted in enrichment of the epithelial mesenchymal transition (EMT) signature for HF2303 but not for HF2927 (Fig 7), consistent with the transcriptional subclasses affiliation, mesenchymal for HF2303 and classical for HF2927 (Fig 1A). We have shown that receptor dependent SMAD1/3/8 are activated in all SDCs (Fig. 2A), consistent with the use of BMP4 to induce the differentiation of iPSC into astrocytes [35]. In agreement, inhibitor of DNA binding 1 (*ID1*), *ID2* and *ID3*, BMP/retinoic acid inducible neural specific 1 (*BRINP1*), downstream of BMP signaling, were upregulated in HF2927 SDCs (Fig 7). Several components of the TGFβ superfamily signaling were upregulated in HF2303 SDCs, including transforming growth factor beta receptor 2 (*TGFBR2*), *BMP1*, latent transforming growth factor beta binding protein 1 (*LTBP1*), *LTBP3*, *SMAD3*, *SMAD9* (Fig 7, S2 Table). On the other hand, endogenous *BMP4* mRNA was downregulated and BMP antagonists DAN family BMP antagonist (*NBL1*) and BMP and activin membrane bound inhibitor (*BAMBI*) were upregulated in HF2303 SDCs, suggesting a possible negative feedback loop, specific for this model. *BAALC*, a regulator of developing neuroectoderm tissues overexpressed in acute leukemia and GBM [64], and a target of SOX2 in differentiated GBM cells [31], is upregulated in HF2303 SDCs (Fig 7). Toll like receptor 4 (*TLR4*), which is expressed in both immune and neoplastic cells, was upregulated in HF2303 SDCs (Fig 7), in agreement with previous studies [65]. *HIF1A* and downstream hypoxia markers were uniquely upregulated in HF2927 SDCs, under normal O2 levels (Fig 7), and the only IFN responsive gene upregulated upon differentiation in this line (Table 1).

Table 1. Differentially expressed genes associated with IFN response and signatures.

	IFN associated pathway and gene signatures					DEG in response to RT or TMZ		DEG in response to differentiation state	
Gene Symbol	**TCGA IFN response correlation group (a)**	**M5911 Hallmark IFN alpha response (b)**	**M5913 Hallmark IFN gamma response (b)**	**IRSD (c)**	**IFN/STAT1 survival proneural (d)**	**Upregulated**	**Downregulated**	**Up SDC**	**Down SDC**
ACSL5	1	0	0	0	0	HF2927 SDC TMZ	0	0	0
ODF3B	1	0	0	0	0	HF2927 SDC TMZ	0	0	0
NEAT1	0	0	0	1	0	HF2927 SDC TMZ	0	0	0
SECTM1	0	0	1	0	0	HF2927 SDC TMZ	0	0	0
OASL	1	1	1	1	0	HF2927 CSC TMZ HF2927 SDC TMZ	0	0	0
CDKN1A	0	0	1	0	0	HF2927 CSC TMZ HF2927 SDC TMZ	0	HF2303	0
RSAD2	1	1	1	0	0	HF2927 CSC TMZ HF2303 SDC TMZ	0	0	0
CMPK2	1	1	1	0	0	HF2927 CSC TMZ	0	0	0
CXCL10	1	1	1	1	0	HF2927 CSC TMZ	0	0	0
EPSTI1	1	1	1	0	0	HF2927 CSC TMZ	0	0	0
DHX58	1	1	1	0	0	HF2927 CSC TMZ	0	0	0
MX2	1	0	1	1	0	HF2927 CSC TMZ	0	0	0
ISG15	1	1	1	1	0	HF2927 CSC TMZ	0	HF2303	0
TRIM22	1	0	0	0	0	HF2927 CSC RT HF2927 CSC TMZ HF2927 SDC TMZ	0	0	0
MX1	1	1	1	1	1	HF2927 CSC RT HF2927 CSC TMZ HF2303 CSC RT HF2303 SDC TMZ	0	HF2303	0
IFI6	1	0	0	1	0	HF2927 CSC RT HF2927 CSC TMZ	0	HF2303	0
OAS2	1	0	1	0	0	HF2927 CSC RT	0	0	0
HERC6	1	1	1	1	0	HF2927 CSC RT	0	0	0
IFI44L	1	1	1	1	0	HF2927 CSC RT	0	0	0

HLA-E	1	0	0	0	0	HF2927 CSC RT	0	HF2303	0
OAS1	1	1	0	1	1	HF2303 SDC TMZ	0	0	0
OAS3	1	0	1	1	0	HF2303 SDC TMZ	0	0	0
SAMD9L	1	1	1	0	0	HF2303 SDC TMZ	0	0	0
GIMAP2	1	0	0	0	0	0	HF2927 SDC TMZ	0	0
TNFAIP3	0	0	1	0	0	0	HF2927 SDC TMZ	0	0
THBS1	0	0	0	1	0	0	HF2927 SDC TMZ	0	HF2927
TNFAI P6	0	0	1	0	0	0	HF2927 SDC TMZ	0	HF2927
HLA-B	1	0	1	1	0	0	HF2303 SDC RT	HF2303	0
IGF2	0	0	0	1	0	0	HF2303 CSC RT	0	0
MTHFD2	0	0	1	0	0	0	0	0	HF2303
IFIT3	1	1	1	1	1	0	0	HF2303	0
BST2	1	1	1	1	0	0	0	HF2303	0
IFI44	1	1	1	1	1	0	0	HF2303	0
RIGI	1	0	1	0	0	0	0	HF2303	0
IRF9	1	1	1	0	0	0	0	HF2303	0
IFIT2	1	1	1	0	0	0	0	HF2303	0
IFITM1	1	1	0	1	0	0	0	HF2303	0
PLSCR1	1	1	1	1	0	0	0	HF2303	0
PLAAT4	1	0	0	0	0	0	0	HF2303	0
HLA-C	1	1	0	0	0	0	0	HF2303	0
LGALS3BP	1	1	1	1	0	0	0	HF2303	0
CA2	0	0	0	1	0	0	0	HF2303	0
ARL4A	0	0	1	0	0	0	0	HF2303	0
BTG1	0	0	1	0	0	0	0	HF2303	0
C1R	0	0	1	0	0	0	0	HF2303	0
CCL2	0	0	1	0	0	0	0	HF2303	0
FGL2	0	0	1	0	0	0	0	HF2303	0
ICAM1	0	0	1	0	0	0	0	HF2303	0
MVP	0	0	1	0	0	0	0	HF2303	0
NAMPT	0	0	1	0	0	0	0	HF2303	0
PELI1	0	0	1	0	0	0	0	HF2303	0
UPP1	0	0	1	0	0	0	0	HF2303	0
MT2A	0	0	1	0	0	0	0	HF2303	HF2927
HIF1A	0	0	1	0	0	0	0	HF2927	0
(a) See S3_Table); (b) https://www.gsea-msigdb.org/; (c) ref. [65]; (d) ref. [70]									

Transcriptional dynamics in response to sublethal treatment with temozolomide and radiation is determined by genomics and differentiation state.

To compare the transcriptional response to temozolomide treatment at distinct differentiation states, GBM cells were treated in triplicate with the respective TMZ IC40

concentrations, calculated from dose-response curves in Fig 5B: 58 μM (HF2303 CSC), 25 μM (HF2927 CSC), 134 μM (HF2303 SDC), 70 μM (HF2927 SDC), or equivalent DMSO control for 4 days. Cells were then harvested and total RNA isolated and sequenced. Differentially expressed genes between treated and control samples for each model and culture type were determined as described for Fig. 7 (C and D in S2 Table). Transcriptional response to 4-day TMZ treatment was largely regulated by wt p53 activation in HF2927 cells (Fig. 8A). We observed that the 18 out of 36 genes commonly upregulated in HF2927 CSCs and SDCs in response to TMZ treatment (Table 2) were validated, direct transcriptional targets of p53 [55]. However, HF2927 differentiation state also influenced p53 transcriptional specificity, as 23 and 26 p53 target genes were significantly upregulated in response to TMZ exclusively in CSCs or SDCs, respectively (Table 2). In contrast, interleukin-27 (IL-27) mediated signaling pathway was enriched in HF2303 SDC in response to TMZ (Fig 8A), based on the upregulation of Myxovirus resistance dynamin like GTPase 1 (*MX1*), 2' 5' oligoadenylate synthetase 1 (*OAS1*) and *OAS2*, all of which are members of the IRDS [63], underlining the cooperation between IL-27 and IFN signaling previously described [66] in response to DNA damage. To identify other components of IFN signaling in GBMs, we identified 100 genes with expression highly correlated to *OAS1* (Spearman's r > 0.55; q value < 5.0E-12) in the TCGA GBM data set (CBIOPortal [67], accessed on 01/19/24). 62% of these genes are members of the hallmark IFN alpha or gamma response pathways, 24% are members of the IRDS [63], and include the 7-gene IFN/STAT1 prognostic signature proposed for GBM proneural subtype [68] (S3 Table). We observed activation of IFN response in TMZ-treated HF2927 CSCs and SDCs, and in HF2303 SDCs (Fig 8A, Table 1). TMZ treatment induced expression of ECM components, and several neural developmental growth and survival factors, including brain derived neurotrophic factor (*BDNF*) and glial cell derived neurotrophic factor (*GDNF*), in HF2927 CSCs and SDCs (Fig 8A). Other neural development associated genes were down regulated in TMZ treated HF2927: platelet

derived growth factor receptor alpha (*PDGFRA*), *OLIG2*, and prominin 1 (*PROM1*) in SDCs; neuropilin 1 (*NRP1*), GLI family zinc finger 1 (*GLI1*), and Kruppel like factor 9 (*KLF9*) in CSCs (Fig 8A). *CDKN1A* (p21), the main effector of p53-mediated downregulation of cell cycle genes, leading to cell cycle arrest, was upregulated in response to TMZ in both HF2927 CSCs and SDCs (Fig 8A,D), but downregulation of cell cycle genes in SDCs was more pronounced (Fig 8A), consistent with corresponding upregulation of Lin-37 DREAM MuvB core complex component (*LIN37*), required for transcriptional repression by DREAM complex downstream of p53 signaling [69], in SDC but not in CSC (Fig 7). One possible explanation for this difference is that cell cycle arrested TMZ-treated HF2927 CSCs may have undergone apoptosis to a larger extent at the time point analyzed, since they demonstrated increased sensitivity to the treatment. Genes coding for proteins involved in EMT, including the master regulator twist family bHLH transcription factor 1 (*TWIST1*), were upregulated in response to TMZ exclusively in HF2927 SDCs, which could contribute to the increased resistance of the differentiated cells.

Fig 8. Transcriptional response to genotoxic treatment in glioblastoma cells. Differentially expressed genes between treated and control samples were determined and enrichment performed as described for Fig. 7. **A)** Transcriptional changes in CSCs and SDCs in response to 4-day TMZ treatment (IC40 concentrations). **B)** Transcriptional changes in CSCs and SDCs measured 5 days after one dose radiation (4 Gy). **C)** RNA commonly downregulated in HF2303 CSCs in response to differentiation and RT treatment. **D)** mRNA expression (RPKM) of p53 transcriptional targets CDKN1A (p21), MDM2, and BBC3, and of cell cycle regulators in HF2303 and HF2927 control and treated cells, mean and SE of n=3. Figures created with Biorender.com.

Table 2. Genes upregulated in HF2927 cells in response to temozolomide.

Validated p53 direct targets			**Other**
CSC & SDC	**CSC**	**SDC**	**CSC & SDC**
ABCA12	*ALDH1A3*	*APOBEC3C*	*ABCA1*
ACER2	*ASTN2*	*CATSPERG*	*ANK1*
BBC3	*CEL*	*CES2*	*APLP1*
CDKN1A	*CLCA2*	*CGB7*	*BDNF*
COL7A1	*DRAM1*	*DDB2*	*CARNS1*
CPE	*EDA2R*	*EML2*	*F11R*
DGKA	*FAM13C*	*GPX1*	*FOXI3*
EPS8L2	*HES2*	*IGFBP7*	*FST*
FDXR	*KLHDC7A*	*MR1*	*GALNT5*
GDF15	*LAPTM5*	*MYOF*	*GDNF*

KITLG	*LIF*	*NINJ1*	*HKDC1*
PLK3	*MAST4*	*NKAIN4*	*INPP5D*
SERPINE1	*MDM2*	*PARD6G*	*IP6K3*
SPATA18	*NEFL*	*PGF*	*KIAA1217*
SULF2	*PDE4C*	*PHLDA3*	*KISS1R*
TP53I3	*PLCL2*	*PIDD1*	*LYNX1*
TRIM22	*PRDM1*	*PLXNB2*	*MARCH11*
WDR63	*RGS16*	*PRKX*	*MUC19*
	RRM2B	*RGMA*	*NECTIN4*
	SESN1	*RRAD*	*NEURL1*
	SYTL1	*SCN2A*	*NR5A1*
	TP53INP1	*SCN4B*	*NTN1*
	VWCE	*SESN2*	*OASL*
		TNFRSF10C	*PDGFC*
		TSPAN11	*PROCR*
		UNC5B	*SLC52A1*
			SMIM10L2A
			STC2
			TMEM80

Ionizing radiation can damage molecules directly, exerting most of its toxicity to cancer cells through DNA double strand breaks (DSBs), and indirectly through the generation of free radicals. The complex cellular responses leading to cell cycle arrest, apoptosis, DNA repair and other processes occur over time [70]. The relative sensitivity of glioblastoma cells to RT varied according to tumor of origin but not according to differentiation status under the experimental parameters employed here (Fig 6A). Furthermore, pre-implantation treatment with 4Gy led to delayed xenograft tumor growth for all models (Fig 6B). To integrate these observations with cellular responses, CSCs and SDCs were treated in triplicates with 4 Gy radiation dose or mock radiation control, followed by incubation in the respective growth media for 5 days prior to RNA isolation and sequencing. Under these conditions, few transcripts were altered in response to RT in HF2303 (Fig 8B), consistent with the resistance to 4 Gy dose observed for both SDCs and CSCs (Fig 6A). The only transcripts commonly upregulated in HF2303 CSCs and SDCs in response to RT were phospholipase C eta 2 (*PLCH2*) and *SNORD3D* (Fig 8B). Interestingly, 50 of the pseudogenes involved in negative regulation of the execution phase of apoptosis

downregulated in response to differentiation of CSCs into SDCs (Fig 7), were also downregulated in RT-treated HF2303 CSCs (Fig 8B,C). Fewer IFN response genes were upregulated in RT treated cells, compared to TMZ treatment, including *MX1* which was upregulated in both CSC lines, and *OAS2*, *HERC6*, *IFI44L* and *HLA-E* in HF2927 CSCs (Table 1, Fig 8B). In contrast to the response to TMZ, where the cells were analyzed after 4 days of continuous treatment (Fig 8A), p53-mediated signaling in HF2927 was more attenuated 5 days after RT, as expected (Fig 8B). Few p53 transcriptional targets remained elevated in irradiated HF2927 cells, such as BCL2 Binding Component 3 (*BBC3 / PUMA*), a pro-apoptotic BCL-2 family member, while expression of several others, including *MDM2*, were not altered at the 5-day timepoint (Fig 8B,D). *CDKN1A*/p21, the main effector of p53 mediated cell cycle arrest significantly upregulated in response to TMZ (Fig 8A), was elevated to a lesser degree in response to RT, below the statistical threshold employed to determine DEGs (Fig 8D). Yet, sustained downregulation of cell cycle genes downstream of p53 activation was observed in RT-treated HF2927 CSCs and SDCs (Fig 8B). Indeed, the majority of the 56 transcripts commonly downregulated in HF2927 CSC and SDCs in response to RT code for cell cycle components (Table 3). Interestingly, forkhead box M1 (*FOXM1*), a transcriptional activator of cell cycle genes, especially those involved in G2 and M phases [71], including Polo-like kinase 1 (*PLK1*) which phosphorylates and activates FOXM1 in a positive feed-back loop [72], were downregulated exclusively in RT-treated cells at the time point analyzed (Fig. 8B,D). Furthermore, DNA damage response and double strand break repair genes were downregulated in response to RT predominantly in HF2927 CSCs (Fig 8B), indicating that these cells would be sensitized to subsequent DNA damaging interventions.

Table 3. Genes downregulated in HF2927 CSC and SDC in response to radiation.

RT CSC/SDC	RT CSC/SDC & TMZ SDC	RT CSC/SDC & TMZ CSC/SDC
AURKB	*ASPM*	*CDC20*
BIRC5	*AURKA*	*KIF20A*

CCNA2	*BUB1*	
CCNB2	*BUB1B*	
CDCA2	***CCNB1***	
DEPDC1	*CDCA8*	
ESPL1	*CENPE*	
FOXM1	*CEP55*	
GTSE1	*DLGAP5*	
HIST1H1B	*GAS2L3*	
HJURP	*HIST1H2AB*	
HMGB2	*HIST1H2AJ*	
HMMR	*HIST1H2AL*	
IQGAP3	*HIST1H2BB*	
KIF15	*HIST1H2BO*	
KIF23	*HIST1H3F*	
KIF2C	*HIST1H3G*	
MELK	*KIF11*	
NEK2	*KIF14*	
NUSAP1	*KIFC1*	
PIMREG	*KNL1*	
PRC1	*MKI67*	
PTTG1	*NCAPH*	
RRM2	*NUF2*	
TROAP	*PBK*	
UBE2C	***PLK1***	
	TPX2	
	TTK	
(*) Genes in bold belong to the FOXM1 pathway		

DNA methylation alteration pattern in differentiation of CSCs

To verify the contribution of epigenetic regulation to the transcriptional responses reported above, we analyzed the global DNA methylation profile of control and treated HF2303 and HF2927 CSCs and SDCs in triplicates, using Infinium Human Methylation 450K BeadChip. Differences in DNA methylation distinguished the samples according to the tumor of origin (HF2303 vs HF2927), as shown in the t-SNE plot (Fig 9A). Analysis of the differentially methylated probes (DMP) and regions (DMR) between CSC and SDC for each of these models, identified 892 DMP and 12 DMRs for HF2303, and 27,431 DMP and 2 DMRs for HF2927 (S4

Table). Similar to the significant overlap in DEGs associated with CSC differentiation between the two cell lines (Fig 7, Fig 9B), we identified 384 DMPs common to both lines (Fig 9B, S4 Table), with a pattern of decreased β-values in SDCs relative to CSCs in HF2303 while HF2927 SDCs exhibited an increase in β-values. The intersection between genes mapped to the DMPs, at the transcription start sites or CpG islands, and the genes differentially expressed between CSCs and SDCs were limited to 17 and 59 genes for HF2303 and HF2927, respectively. Among these genes, latent transforming growth factor beta binding protein 3 (*LTBP3*) was associated with DMPs and upregulation in SDC for both models (Fig 9B, S4 Table). Cholesterol homeostasis, hypoxia, growth factor binding and ECM components were significantly represented in the 59 gene list from HF2927 (S4 Table). No significant DNA methylation changes were observed in the acute response to RT and TMZ treatment in any of the cell lines or differentiation states (S4_Fig).

Fig 9. Genome-wide DNA methylation profiling groups samples by patient of origin and identifies DNA methylation alteration patterns between glioblastoma CSCs and their differentiated progeny. A) t-SNE plot from b-values for all CpG sites comparing HF2303 and HF2927 CSCs and SDCs treated with control, RT or TMZ, in triplicates. **B)** Schematic showing the significant intersect for HF2303 and HF2927 of differentially expressed genes (DEGs) and differentially methylated probes (DMPs) between CSCs and SDCs. The intersect between DMPs annotated to genes (see Methods) and DEGs are shown. Significance of the intersections was determined using GeneOverlap, p-values and estimated odds ratio are shown; n.s., nonsignificant. **C)** Heatmap showing the b-values for the 387 DMPs common to HF2303 and HF2927. Figure 9B created with Biorender.com.

Discussion

Our results show that patient specific GBM genomic landscapes have a significant impact in CSCs differentiation pathways and response to TMZ and RT. The integrated analysis of signaling pathways in multiple GBM models, distinct differentiation states and treatment groups contributed to the identification of candidate therapeutic targets associated with GBM resistance to the standard of care. Employing targeted proteomics, we quantified shifts in the steady-state levels of key oncogenic signaling components following a 2-week exposure of CSCs to astrocytic differentiation (SDCs), growth factor withdrawal, or traditional culture media

supplemented with 10% FBS. The cell state-dependent alterations in cell signaling were not uniform among the different cell lines, but a few common patterns emerged, such as the activation of BMP-Smad in the presence of FBS, both in SDCs (2%) and in 10% FBS. Confirming these findings, transcriptional targets of r-Smad1/5/8 were upregulated in HF2303 and HF2927 SDCs. This is in agreement with BMP signaling inducing astrocytic differentiation of patient-derived oligodendroglioma cells [73], and with BMP ligands being present in FBS [38]. PI3K/AKT/mTOR hyperactivation supporting cell growth, proliferation and survival, a hallmark of glioblastoma [74], was observed in 7/8 CSCs and SDCs, and decreased upon withdrawal of growth factors, as expected. AKT activation was most strongly correlated with the inhibitory phosphorylation of GSK3α/β at S21/S9 in this dataset. RTK and MAPK pathways activation was remarkably higher in SDC relative to other conditions for all GBM lines, except for the two carrying ecDNA EGFR amplification (HF2927 and HF3016), consistent with a role for MAPK in early astrocytic differentiation [75]. The representation of various genomic backgrounds and external stimuli in the targeted proteomics dataset provided insights into the complex signaling networks co-activated in GBMs. Non-receptor tyrosine kinase Src is a node of convergence for receptor mediated signaling pathways, activating substrates in the MAPK, JAK/Stat3, and PI3K/AKT pathways to promote tumor cell survival, proliferation and invasion in various cancers, including GBMs [76]. Our data show that levels of activating Src phosphorylation at the Y416 residue did not correlate with the canonical upstream and downstream signaling, including phospho-Stat3, but presented a strong correlation with the inhibitory phosphorylation of the Y529 residue. Consistent with our observations, this bi-phosphorylation of Src has been previously reported to reflect an intermediate state between open and closed kinase conformations with blockage of the SH3 domain leading to limited Stat3 phosphorylation activity, suggesting that additional stimulatory factors are required for downstream signaling [77]. Phospho-Stat3 (S727) in this data set was more highly correlated with activated mTORK1 and MAPK pathways, as expected. Weighing the relationship of genomic drivers and cell state, a

comparable study specifically exploring CSC/SDC characteristics in the presence and absence of radiation, or alkylating therapy, postulated that cell state superseded genetic makeup with respect to growth dynamics and treatment resistance [78]. One critical difference in this study to previous paired CSC/SDC comparisons was the utilization of a lower serum consideration that is conducive for the maintenance of developmental plasticity under differentiated conditions [79]. Culturing CSCs in the traditional media supplemented with 10% FBS resulted in suppression of other key oncogenic signaling for all 8 CSCs, providing further evidence that this media is not conducive to preserving GBM original characteristics, as previously reported [33, 50]. With respect to the individual CSC models, we show that the genomic background is vital to a cell's ability to adapt to different conditions and hence establish the different cell states (CSCs, SDCs). In response to cytotoxic agents, the resistance phenotype, independent of cell state, was attributed to either autonomous interferon signaling or cell cycle arrest through intact p53 signaling.

Transcriptional reprograming associated with the differentiation of CSCs into SDCs revealed two commonly altered cellular functions in the GBM models analyzed, HF2303 and HF2927. Cholesterol biosynthesis was enriched in CSCs, with evidence for transcriptional activity of sterol regulatory element binding proteins (SREBPs), in response to the lack of cholesterol in the serum-free neurosphere media. Because GBM cells tend to uptake cholesterol from the brain microenvironment [56] and cholesterol is a component of FBS, cholesterol biosynthesis was downregulated in SDCs (2% FBS). ECM components, receptors and regulators were upregulated in SDCs, resembling transcriptional regulation of ECM components in astrocytes [61], likely with contribution of stimulatory attachment factors in FBS. The enrichment in ECM-receptor interaction observed for SDCs is associated with treatment resistance GBMs [80], and could be a factor contributing to the increased resistance of GBM SDCs to TMZ treatment. The retention of the expression of key stemness signature genes in SDCs, including *SOX2* and several of its transcriptional targets, highlights the role of these

genes in the maintenance of developmental plasticity in more differentiated GBM cells, as we previously reported [31]. Other aspects of the transcriptional reprograming associated with differentiation of CSCs were model specific. We had previously shown that NF1 mutant HF2303 CSCs, like its parental tumor, belongs to the mesenchymal subclass and can recapitulate the biphasic gliosarcoma phenotype in orthotopic mouse xenografts [31]. Here, we show that CSC differentiation for this model resulted in enrichment of EMT signature, analogous to the mesenchymal cell state in NF1-deficient GBM [15]. DNA methylation alterations associated with CSC differentiation varied, with 30-fold more DMPs identified for HF2927 relative to HF2303, but the intersect between the 2 lines was highly significant at CpG level, but not at DMR level. On the other hand, under the experimental conditions employed in this study, we did not observe significant changes in global DNA methylation in response to treatment. There is no consensus in the occurrence and extent of changes in global DNA methylation patterns in response to ionizing radiation or temozolomide treatment in cultured cells [81]. This is in part due to the variability in cell intrinsic factors, such as cell type, genomic alterations, proliferation rate and cell cycle phase, as well as extrinsic factors, including culture conditions, radiation and temozolomide dosage and schedule.

We observed that differentiation of CSCs into SDCs increased resistance to TMZ for all three models tested, two representing unmethylated and one methylated MGMT promoter. We show that baseline MGMT protein levels are strongly correlated with the level of NF-κB activation in MGMT promoter methylated and unmethylated GBM cells, supporting previous reports that NF-kB activation confers resistance to DNA-alkylating agents mainly through regulation of MGMT in glioma [7]. Previous studies attributed GBM CSCs with increased DNA repair capacity and corresponding resistance to radiation when compared to “non-CSCs”, where “CSCs” and “non-CSCs” were defined by the presence of cell surface markers (e.g. CD133) and cultured in different media immediately after tumor dissociation [82]. In contrast, using a different paradigm in this study, where CSCs are obtained through selective media enrichment,

and subsequently differentiated into SDCs, we report that sensitivity to clinically relevant doses of RT was unchanged between CSCs and their differentiated progeny SDCs. The status of *TP53*, a key regulator of cellular response to DNA-damaging agents, was not surprisingly a key determinant of the transcriptional response of the GBM models to TMZ and RT. HF2927 carries wt TP53 while HF2303 carries TP53 G245S, a dominant negative mutation which disrupts the structure of p53 DNA binding domain, impairing p53 transcriptional activity [83]. Our data also demonstrates the temporal and context specificity of wt p53 target genes in the same model. We report the upregulation of direct targets of p53 only in HF2927 cells continually treated with TMZ, while when measured 5 days after RT, p53 targets were no longer upregulated. Downregulation of cell cycle genes by p53 in response to DNA-damage, accomplished indirectly through the DREAM complex, was observed for wt p53 HF2927 CSCs and SDCs in response to continuous TMZ treatment. *FOXM1*, a transcriptional activator of cell cycle genes, especially those involved in G2 and M phases, is downregulated by tumor suppressors p53 and Rb and frequently overexpressed in various cancers [71]. We show that *FOXM1* was highly expressed in untreated HF2303 and HF2927 cells. Although p53 target genes, including *CDKN1A*/p21 were no longer upregulated 5 days after RT-treatment, we observed downregulation of *FOXM1* and components of the pathway it regulates exclusively in response to RT treatment of HF2927, in both CSCs and SDCs at this timepoint.

Best known for its effect in triggering innate immune response, accumulation of cytoplasmic ssDNA or dsDNA in cancer cells following DNA damage activates cGMP-AMP synthase (cGAS)–stimulator of IFN genes (STING) pathway, leading to the activation of type I IFN production and upregulation of IFN-stimulated genes (ISGs) [84]. Some ISGs have known radioresistance functions in suppressing interferon production, through a negative feedback mechanism, [85] and the type I interferon response sensitizes p53-deficient cells in response to chemotherapy [86]. Conversely, IRDS is a subset of ISGs induced by prolonged exposure to low doses of type I interferons [87], and associated with resistance to radiation in various cancers

[63]. *OAS1*, involved in resistance to alkylating therapy [88] and a member of the IRDS [63], is a component of the IFN/STAT1 prognostic signature proposed for GBM proneural subtype [68]. Because IFN response is coordinated and typically presents a high degree of correlation in gene expression, our analysis identified genes highly correlated with expression to *OAS1* in the TCGA GBM dataset. Upregulation of these IFN responsive genes was overrepresented in response to TMZ and RT treatment of GBM CSCs and SDCs. Differentiation of HF2303 CSCs was characterized by upregulation of IFN pathway genes. This is consistent with reports that cancer cell-intrinsic type I IFN signaling is inversely correlated to stemness in a pan-cancer study [89]. We did not observe this IFN activation in HF2927 SDCs cells, highlighting the heterogeneity of responses of GBM CSCs to external stimuli. Others have shown a chemo-resistant effect of STAT1 suppression in classical GBM CSCs [90] and chemosensitivity associated with upregulated of interferons in p53-deficient setting [86]. Our results highlight the importance of the IFN pathway activation in modulating response to the standard of care, warranting further exploration as a therapeutic target and predictive biomarker.

It is important to note the cross talk among cancer cell subpopulations in different cell states, and interactions with tumor microenvironment host cells add layers of complexity beyond the scope of this study. By analyzing the response to treatment and differentiation in bulk patient-derived GBM cell populations, reflecting the sum of the dynamic alterations in CSCs and SDCs sub-compartments, we uncovered a complex cross talk among oncogenic signaling pathway on GBMs, and show that astrocytic differentiation of CSCs maintains some of the stemness, necessary to maintain plasticity characteristic of high grade tumors, while acquiring properties associated with more differentiated GBM cells, such as activation of BMP/Smad, metabolic switches, and production of ECM. Although our approach is limited to neoplastic cells and does not examine the effect of therapy interactions on the entire tumor milieu, experimental modeling of distinct differentiation states is relevant for pre-clinical work, and the integrated molecular analysis presented here provides the proper context for future studies. The aspects of

reprograming that were tumor specific indicate that caution is warranted in generalizing findings pertaining to the differentiation of CSCs or their sensitivity and molecular response to treatment across diverse glioblastoma models. Our work supports further evidence to the potential of targetable pathways to sensitize GBMs to the standard of care, such as the IFN response.

Methods

Cell culture

Glioblastoma patient-derived cancer stem cell cultures were obtained from the live biobank collection at the Hermelin Brain Tumor Center, Henry Ford Hospital (Detroit, MI). These cells were derived from de-identified surgically resected glioblastoma specimens, collected with written informed consent, under a protocol approved by the HFH Institutional Review Board as previously described [79], in compliance with all relevant ethical regulations for research using human specimens. Cells were cultured in serum-free neurosphere media consisting of Dulbecco's Modified Eagle Medium (DMEM)/F12 media (Invitrogen), N2 supplement (Gibco) and 0.5 mg/ml BSA, supplemented with growth factors 20 ng/ml EGF and 20 ng/ml bFGF (Peprotech) (NMGF), to select for CSCs [79]. CSC cultures were passaged in vitro and used prior to achieving passage 20. Identity of CSC lines was confirmed by comparing genotype with the patient germline using Short Tandem Repeat (STR) analysis. CSCs were dissociated and cultured for 2 weeks in three different conditions: NM lacking growth factors, and NMGF supplemented with 2% or 10% FBS (HyClone). Neural progenitor cells (NPCs) were derived from H9 human ESC, obtained from WiCell (Madison WI) as described [91] and differentiated in NMGF supplemented in 2% FBS [92].

Reverse Phase Protein Arrays analysis

Cell lysates were obtained in triplicate for each cell line and growth conditions described (Fig 1B). The levels of 66 proteins/post-translational modifications in the cell lysates were analyzed by Reverse Phase Protein Arrays (RPPA) at the Mason's Center for Applied Proteomics and Molecular Medicine (George Mason University), essentially as described previously [36, 37]. Statistical analyses of RPPA normalized values were conducted in the R statistical environment (4.2.1). Heatmaps were generated by ComplexHeatmap package in R (2.12.1) [93]. Z-scores for each protein and post-translational modification were calculated based on population mean and standard deviation ($(x-\mu)/\sigma$). Fold-change was calculated using the gTools package (3.9.3) and computed as follows: num/denom if num>denom, and as -denom/num otherwise. Dendrograms were produced using Spearman correlation as the distance method.

Cell proliferation, radiation and temozolomide treatment

Cell proliferation*:* Cell proliferation curves were established by plating 1,000 cells/well into 96-well plates in NMGF (CSCs) or NMGF supplemented with 2% FBS (SDCs) and measuring cell viability after 1, 4, 6, 8, and 11 days in culture (n=5). Wells were supplemented with fresh media every 3-4 days. Cell viability was measured using CellTiter-Glo Luminescent Cell Viability Assay (Promega), relative light units (RLU) were measured in a BioTek Cytation 3 plate reader. Doubling time (DT) was calculated using the formula $DT=(t1-t2)\ln 2 / \ln(RLU2/RLU1)$.

Temozolomide dose-response curves*:* CSCs and SDCs were plated in 96-well assay plates (3,000 cells/well), in quintuplicates and treated with 10 to 400 μM temozolomide (Schering-Plough) or DMSO control for 4 days. CellTiterGlo (Promega) was used to measure cell viability and dose-response curves were generated by non-linear fitting, IC50 doses and area above the curve (AAC) were calculated in GraphPad Prism (v.9.0).

Ionizing radiation treatment (RT): CSC and SDC cells were dissociated, irradiated with 0, 2 or 4 Gy using a 5000 Ci Cesium (Cs-137) irradiator, and plated in triplicate at density of 3,000

761 cells/well in 96-well assay plates in the respective growth media and incubated under standard
762 conditions for 5 days. Cell viability was assayed with CellTiter Glo (Promega). Surviving
763 fractions at the two radiation doses were calculated and compared.
764 Tumorigenic potential of irradiated cells: Single cell suspensions of glioblastoma CSCs
765 constitutively expressing firefly luciferase were irradiated with 0 (mock) or 4Gy, as described
766 above. Immediately following radiation or control treatment, $2x10^5$ cells/mouse were implanted
767 intracranially in female NCRNU-M athymic nude mice (Taconic Farms) as described [94]. Mice
768 were monitored by bioluminescence imaging using IVIS and sacrificed when presenting
769 symptoms associated with tumor burden.
770 Sublethal temozolomide and radiation treatment for total RNA and genomic DNA isolation:
771 *Temozolomide*: GBM CSCs or SDCs growing in their respective media were treated in triplicate
772 with the respective TMZ IC40 concentrations or control DMSO for 4 days. *Radiation*: Cells were
773 treated in triplicate with ionizing radiation (4Gy) or mock radiation control (0Gy) and cultured for
774 5 days. For all treatment groups, cells were harvested, total RNA isolated using RNeasy Mini Kit
775 (Qiagen) and used for RNA sequencing. Genomic DNA was isolated using QIAamp DNA kit
776 (Qiagen) and used for DNA methylation profiling.
777

778 RNA Sequencing

779 RNA quality assessment was performed using the Agilent RNA ScreenTape on the Agilent 2200
780 TapeStation. Library for RNA sequencing was prepared using TruSeq Stranded Total RNA LT
781 (Illumina). 100 bps paired-end libraries were sequenced on the Illumina HiSeq 2500 following
782 cBot clustering. Prior to alignment the sequencing adaptors were trimmed using FASTQ Toolkit
783 v1.0 on Illumina's BaseSpace portal. FastQC was used to generate quality metrics for
784 assessment of FASTQ files [95]. RNA seq reads were aligned using TopHat v2.1.0 using default
785 alignment parameters and GRCh38 reference genome [96, 97]. After alignment, the mapped

reads were further filtered by mappability score (MAPQ ≥ 10) and sorted by genomic position of the reads using samtools-0.1.19 [98]. PCR duplicate reads were processed and removed using rmdup function (options -S) in samtools. The cleaned BAM files were further analyzed using Integrative Genome Viewer (http://software.broadinstitute.org/software/igv/), processed with R function "FeatureCount" to quantify reads on various RNA types from GencodeV28 annotation. Differential gene expression analysis was performed using the non-parametric algorithm "NOISeq" in R **[99]**, with q = 0.8 and fold change >2 or <0.5 thresholds on TMM normalized data for treated vs. control comparisons, and q = 0.8 on RPKM normalized data for long term transcriptome changes in untreated SDCs vs CSCs. Gene set enrichment tests for differentially expressed gene lists were performed using Metascape 3.5, and adjusted p-value (q) < 0.05 [100].

DNA methylation analysis

Genomic DNA was analyzed using Infinium Human Methylation 450K BeadChip system (Illumina), as described [91]. Raw methylation data was pre-processed for dye-bias normalization, detection p-value was calculated by comparing the signal intensity difference between array probes and a set of negative control probes on the array; probes with p-value greater than 0.01 filtered out. Beta values were calculated from pre-processed raw data using methylumi Bioconductor package in R [101]. Probes mapping to known SNPs and sex chromosomes were filtered out of dataset as recommended by Zhou et al. [102]. Beta values were corrected for batch effect using ComBat function within sva R package [103, 104]. Probes were aligned to hg38 and annotated using Illumina methylation 450k manifest [105]. Differentially methylated probes between experimental groups (n=3/group) were determined using champ.DMP function, and to determine differentially methylated regions we used the champ.DMR with Bumphunter method from the ChAMP package in ChAMPs R package [106]

with raw p-values < 0.05, and adjusted p-value < 0.1. DMPs were annotated to genes using illuminaHg19 annotation employed by the ChAMPs package in R. Analyses to determine the intersect of DMPs, the genes mapped to DMPs and DEGs, within and between models, were carried out using GeneOverlap (version 1.34.0).

Cellular oxygen consumption rate

Cellular oxygen consumption rate (OCR) was measured using a Seahorse XF Cell Mito Stress Test in a XFe24 Bioanalyzer (Agilent). Cells were plated at a concentration of 30,000 (HF2303) or 40,000 (HF2927) per well on poly-ornithine hydrobromide (Sigma # 4957) coated plates in NMGF media (CSC) or 2%FBS media (SDC) and treated for 4 days with DMSO or TMZ IC40 concentrations, prior to basal oxygen consumption measurements, performed according to the manufacturer's instructions.

Statistical analysis

Statistical analyses were performed using GraphPad Prism (v. 9.00) or R and are described in the results section for each experiment. Tumor growth in mouse PDX was evaluated by Kaplan-Meier survival curves, compared by the log-rank test with $p<0.05$ considered significant.

Data availability

The data discussed in this publication have been deposited in NCBI's Gene Expression Omnibus [107] and are accessible through GEO Series accession number GSE249637.

Funding

This work was supported by Department of Defense Idea award CA180174 (ACD) and the Demchik Family Fund for Glioma Patient-Derived Avatar Models (ACD). ON received support from NIH F31 CA250450-01, and AB was supported by NIH T32 CA009531 training fellowship (Wayne State University).

Competing Interests

The authors declare no competing interests.

Acknowledgments

We thank Kristyn Quenneville and Dr. Nouman Mughal for their assistance with reviewing and editing the manuscript.

Author contributions

A.C.D. and D.R. conceived the study. K.B., Y.M., S.I., L.H., and A.B. performed cell culture, treatment response, and prepared cell lysate, DNA and RNA for profiling. C.M. and E.F.P. generated the RPPA data and performed initial analysis at Mason's Center for Applied Proteomics and Molecular Medicine (CAPMM). AB performed RPPA data analysis. S.B. performed the radiation experiments. KG and DR performed the RNA sequencing and DNA Methylation at the Wayne State University Genomics Core. ID, LP and ON performed the RNAseq bioinformatics analysis. OD, TS and HN performed the DNA methylation bioinformatics analysis. N.P. and S.A. performed the OCR measurements. A.C.D., A.B. and O.N wrote the manuscript with input from co-authors.

References

1. Louis DN, Perry A, Wesseling P, Brat DJ, Cree IA, Figarella-Branger D, et al. The 2021 WHO Classification of Tumors of the Central Nervous System: a summary. Neuro-oncology. 2021;23(8):1231-51. Epub 2021/06/30. doi: 10.1093/neuonc/noab106. PubMed PMID: 34185076; PubMed Central PMCID: PMCPMC8328013.
2. Marko NF, Weil RJ, Schroeder JL, Lang FF, Suki D, Sawaya RE. Extent of resection of glioblastoma revisited: personalized survival modeling facilitates more accurate survival prediction and supports a maximum-safe-resection approach to surgery. Journal of clinical oncology : official journal of the American Society of Clinical Oncology. 2014;32(8):774-82. Epub 20140210. doi: 10.1200/JCO.2013.51.8886. PubMed PMID: 24516010; PubMed Central PMCID: PMCPMC4876349.
3. Stupp R, Mason WP, van den Bent MJ, Weller M, Fisher B, Taphoorn MJ, et al. Radiotherapy plus concomitant and adjuvant temozolomide for glioblastoma. The New England journal of medicine. 2005;352(10):987-96. doi: 10.1056/NEJMoa043330. PubMed PMID: 15758009.
4. Marenco-Hillembrand L, Wijesekera O, Suarez-Meade P, Mampre D, Jackson C, Peterson J, et al. Trends in glioblastoma: outcomes over time and type of intervention: a systematic evidence based analysis. Journal of neuro-oncology. 2020;147(2):297-307. Epub 2020/03/12. doi: 10.1007/s11060-020-03451-6. PubMed PMID: 32157552.
5. Hegi ME, Diserens A-C, Gorlia T, Hamou M-F, de Tribolet N, Weller M, et al. MGMT Gene Silencing and Benefit from Temozolomide in Glioblastoma. The New England journal of medicine. 2005;352(10):997-1003.
6. Chen X, Zhang M, Gan H, Wang H, Lee JH, Fang D, et al. A novel enhancer regulates MGMT expression and promotes temozolomide resistance in glioblastoma. Nat Commun. 2018;9(1):2949. Epub 20180727. doi: 10.1038/s41467-018-05373-4. PubMed PMID: 30054476; PubMed Central PMCID: PMCPMC6063898.
7. Lavon I, Fuchs D, Zrihan D, Efroni G, Zelikovitch B, Fellig Y, et al. Novel mechanism whereby nuclear factor kappaB mediates DNA damage repair through regulation of O(6)-methylguanine-DNA-methyltransferase. Cancer Res. 2007;67(18):8952-9. doi: 10.1158/0008-5472.CAN-06-3820. PubMed PMID: 17875738.
8. Hegi ME, Diserens A-C, Gorlia T, Hamou M-F, De Tribolet N, Weller M, et al. MGMT gene silencing and benefit from temozolomide in glioblastoma. New England Journal of Medicine. 2005;352(10):997-1003.
9. Yan H, Parsons DW, Jin G, McLendon R, Rasheed BA, Yuan W, et al. IDH1 and IDH2 mutations in gliomas. New England Journal of Medicine. 2009;360(8):765-73.
10. Noushmehr H, Weisenberger DJ, Diefes K, Phillips HS, Pujara K, Berman BP, et al. Identification of a CpG island methylator phenotype that defines a distinct subgroup of glioma. Cancer cell. 2010;17(5):510-22.
11. Sanchez-Vega F, Mina M, Armenia J, Chatila WK, Luna A, La KC, et al. Oncogenic Signaling Pathways in The Cancer Genome Atlas. Cell. 2018;173(2):321-37. e10.
12. Olson JJ, Nayak L, Ormond DR, Wen PY, Kalkanis SN, Ryken TC. The role of targeted therapies in the management of progressive glioblastoma: a systematic review and evidence-based clinical practice guideline. Journal of neuro-oncology. 2014;118:557-99.
13. Johnson BE, Mazor T, Hong C, Barnes M, Aihara K, McLean CY, et al. Mutational analysis reveals the origin and therapy-driven evolution of recurrent glioma. Science. 2014;343(6167):189-93. Epub 2013/12/18. doi: 10.1126/science.1239947. PubMed PMID: 24336570; PubMed Central PMCID: PMCPMC3998672.

14. deCarvalho AC, Kim H, Poisson LM, Winn ME, Mueller C, Cherba D, et al. Discordant inheritance of chromosomal and extrachromosomal DNA elements contributes to dynamic disease evolution in glioblastoma. Nat Genet. 2018;50(5):708-17. Epub April 23. doi: 10.1038/s41588-018-0105-0. PubMed PMID: 29686388; PubMed Central PMCID: PMCPMC5934307.

15. Neftel C, Laffy J, Filbin MG, Hara T, Shore ME, Rahme GJ, et al. An Integrative Model of Cellular States, Plasticity, and Genetics for Glioblastoma. Cell. 2019;178(4):835-49 e21. Epub 20190718. doi: 10.1016/j.cell.2019.06.024. PubMed PMID: 31327527; PubMed Central PMCID: PMCPMC6703186.

16. Yabo YA, Niclou SP, Golebiewska A. Cancer cell heterogeneity and plasticity: A paradigm shift in glioblastoma. Neuro-oncology. 2022;24(5):669-82. doi: 10.1093/neuonc/noab269. PubMed PMID: 34932099; PubMed Central PMCID: PMCPMC9071273.

17. Reinartz R, Wang S, Kebir S, Silver DJ, Wieland A, Zheng T, et al. Functional Subclone Profiling for Prediction of Treatment-Induced Intratumor Population Shifts and Discovery of Rational Drug Combinations in Human Glioblastoma. Clin Cancer Res. 2017;23(2):562-74. Epub 20160812. doi: 10.1158/1078-0432.CCR-15-2089. PubMed PMID: 27521447; PubMed Central PMCID: PMCPMC5241221.

18. Brennan CW, Verhaak RG, McKenna A, Campos B, Noushmehr H, Salama SR, et al. The somatic genomic landscape of glioblastoma. Cell. 2013;155(2):462-77. Epub 2013/10/15. doi: 10.1016/j.cell.2013.09.034. PubMed PMID: 24120142; PubMed Central PMCID: PMCPMC3910500.

19. Vitucci M, Karpinich NO, Bash RE, Werneke AM, Schmid RS, White KK, et al. Cooperativity between MAPK and PI3K signaling activation is required for glioblastoma pathogenesis. Neuro-oncology. 2013;15(10):1317-29.

20. See WL, Tan I-L, Mukherjee J, Nicolaides T, Pieper RO. Sensitivity of glioblastomas to clinically available MEK inhibitors is defined by neurofibromin 1 deficiency. Cancer research. 2012;72(13):3350-9.

21. Mendoza MC, Er EE, Blenis J. The Ras-ERK and PI3K-mTOR pathways: cross-talk and compensation. Trends Biochem Sci. 2011;36(6):320-8. Epub 20110430. doi: 10.1016/j.tibs.2011.03.006. PubMed PMID: 21531565; PubMed Central PMCID: PMCPMC3112285.

22. Suvà ML, Rheinbay E, Gillespie SM, Patel AP, Wakimoto H, Rabkin SD, et al. Reconstructing and reprogramming the tumor-propagating potential of glioblastoma stem-like cells. Cell. 2014;157(3):580-94.

23. Ignatova TN, Kukekov VG, Laywell ED, Suslov ON, Vrionis FD, Steindler DA. Human cortical glial tumors contain neural stem-like cells expressing astroglial and neuronal markers in vitro. Glia. 2002;39(3):193-206. PubMed PMID: 12203386.

24. Hemmati HD, Nakano I, Lazareff JA, Masterman-Smith M, Geschwind DH, Bronner-Fraser M, et al. Cancerous stem cells can arise from pediatric brain tumors. Proc Natl Acad Sci U S A. 2003;100(25):15178-83. PubMed PMID: 14645703.

25. Galli R, Binda E, Orfanelli U, Cipelletti B, Gritti A, De Vitis S, et al. Isolation and characterization of tumorigenic, stem-like neural precursors from human glioblastoma. Cancer Res. 2004;64(19):7011-21. PubMed PMID: 15466194.

26. Vescovi AL, Galli R, Reynolds BA. Brain tumour stem cells. Nat Rev Cancer. 2006;6(6):425-36. PubMed PMID: 16723989.

27. Shen Y, Grisdale CJ, Islam SA, Bose P, Lever J, Zhao EY, et al. Comprehensive genomic profiling of glioblastoma tumors, BTICs, and xenografts reveals stability and adaptation to growth environments. Proc Natl Acad Sci U S A. 2019;116(38):19098-108. Epub 2019/09/01. doi: 10.1073/pnas.1813495116. PubMed PMID: 31471491; PubMed Central PMCID: PMCPMC6754609.

28. Woo XY, Giordano J, Srivastava A, Zhao ZM, Lloyd MW, de Bruijn R, et al. Conservation of copy number profiles during engraftment and passaging of patient-derived cancer xenografts. Nat Genet. 2021;53(1):86-99. Epub 20210107. doi: 10.1038/s41588-020-00750-6. PubMed PMID: 33414553; PubMed Central PMCID: PMCPMC7808565.
29. Quartararo CE, Reznik E, deCarvalho AC, Mikkelsen T, Stockwell BR. High-Throughput Screening of Patient-Derived Cultures Reveals Potential for Precision Medicine in Glioblastoma. ACS medicinal chemistry letters. 2015;6(8):948-52. doi: 10.1021/acsmedchemlett.5b00128. PubMed PMID: 26288699; PubMed Central PMCID: PMC4538440.
30. Ye LF, Reznik E, Korn JM, Lin F, Yang G, Malesky K, et al. Patient-derived glioblastoma cultures as a tool for small-molecule drug discovery. Oncotarget. 2020;11(4):443-51. Epub 2020/02/18. doi: 10.18632/oncotarget.27457. PubMed PMID: 32064048; PubMed Central PMCID: PMCPMC6996910.
31. Berezovsky AD, Poisson LM, Cherba D, Webb CP, Transou AD, Lemke NW, et al. Sox2 promotes malignancy in glioblastoma by regulating plasticity and astrocytic differentiation. Neoplasia. 2014;16(3):193-206 e25. Epub 2014/04/15. doi: 10.1016/j.neo.2014.03.006. PubMed PMID: 24726753.
32. Zheng X, Baker H, Hancock WS, Fawaz F, McCaman M, Pungor E, Jr. Proteomic analysis for the assessment of different lots of fetal bovine serum as a raw material for cell culture. Part IV. Application of proteomics to the manufacture of biological drugs. Biotechnol Prog. 2006;22(5):1294-300. doi: 10.1021/bp060121o. PubMed PMID: 17022666.
33. Lee J, Kotliarova S, Kotliarov Y, Li A, Su Q, Donin NM, et al. Tumor stem cells derived from glioblastomas cultured in bFGF and EGF more closely mirror the phenotype and genotype of primary tumors than do serum-cultured cell lines. Cancer cell. 2006;9(5):391-403. PubMed PMID: 16697959.
34. Shaltouki A, Peng J, Liu Q, Rao MS, Zeng X. Efficient generation of astrocytes from human pluripotent stem cells in defined conditions. Stem Cells. 2013;31(5):941-52. doi: 10.1002/stem.1334. PubMed PMID: 23341249.
35. Tcw J, Wang M, Pimenova AA, Bowles KR, Hartley BJ, Lacin E, et al. An Efficient Platform for Astrocyte Differentiation from Human Induced Pluripotent Stem Cells. Stem cell reports. 2017;9(2):600-14. Epub 20170727. doi: 10.1016/j.stemcr.2017.06.018. PubMed PMID: 28757165; PubMed Central PMCID: PMCPMC5550034.
36. Mueller C, deCarvalho AC, Mikkelsen T, Lehman NL, Calvert V, Espina V, et al. Glioblastoma cell enrichment is critical for analysis of phosphorylated drug targets and proteomic-genomic correlations. Cancer Res. 2014;74(3):818-28. Epub 2013/12/19. doi: 10.1158/0008-5472.CAN-13-2172. PubMed PMID: 24346432.
37. Pin E, Federici G, Petricoin EF, 3rd. Preparation and use of reverse protein microarrays. Current protocols in protein science / editorial board, John E Coligan [et al]. 2014;75:Unit 27 7. doi: 10.1002/0471140864.ps2707s75. PubMed PMID: 24510676.
38. Kodaira K, Imada M, Goto M, Tomoyasu A, Fukuda T, Kamijo R, et al. Purification and identification of a BMP-like factor from bovine serum. Biochem Biophys Res Commun. 2006;345(3):1224-31. Epub 20060515. doi: 10.1016/j.bbrc.2006.05.045. PubMed PMID: 16716261.
39. Yang G, Murashige DS, Humphrey SJ, James DE. A Positive Feedback Loop between Akt and mTORC2 via SIN1 Phosphorylation. Cell reports. 2015;12(6):937-43. Epub 20150730. doi: 10.1016/j.celrep.2015.07.016. PubMed PMID: 26235620.
40. Efeyan A, Sabatini DM. mTOR and cancer: many loops in one pathway. Curr Opin Cell Biol. 2010;22(2):169-76. Epub 20091127. doi: 10.1016/j.ceb.2009.10.007. PubMed PMID: 19945836; PubMed Central PMCID: PMCPMC2854285.
41. Copp J, Manning G, Hunter T. TORC-specific phosphorylation of mammalian target of rapamycin (mTOR): phospho-Ser2481 is a marker for intact mTOR signaling complex 2. Cancer

Res. 2009;69(5):1821-7. Epub 20090224. doi: 10.1158/0008-5472.CAN-08-3014. PubMed PMID: 19244117; PubMed Central PMCID: PMCPMC2652681.
42. Boutouja F, Stiehm CM, Platta HW. mTOR: A Cellular Regulator Interface in Health and Disease. Cells. 2019;8(1). Epub 20190102. doi: 10.3390/cells8010018. PubMed PMID: 30609721; PubMed Central PMCID: PMCPMC6356367.
43. Ovens AJ, Scott JW, Langendorf CG, Kemp BE, Oakhill JS, Smiles WJ. Post-Translational Modifications of the Energy Guardian AMP-Activated Protein Kinase. Int J Mol Sci. 2021;22(3). Epub 20210127. doi: 10.3390/ijms22031229. PubMed PMID: 33513781; PubMed Central PMCID: PMCPMC7866021.
44. Dite TA, Ling NXY, Scott JW, Hoque A, Galic S, Parker BL, et al. The autophagy initiator ULK1 sensitizes AMPK to allosteric drugs. Nat Commun. 2017;8(1):571. Epub 20170918. doi: 10.1038/s41467-017-00628-y. PubMed PMID: 28924239; PubMed Central PMCID: PMCPMC5603566.
45. Okada M. Regulation of the SRC family kinases by Csk. Int J Biol Sci. 2012;8(10):1385-97. Epub 20121101. doi: 10.7150/ijbs.5141. PubMed PMID: 23139636; PubMed Central PMCID: PMCPMC3492796.
46. Metz HE, Houghton AM. Insulin receptor substrate regulation of phosphoinositide 3-kinase. Clin Cancer Res. 2011;17(2):206-11. Epub 20101021. doi: 10.1158/1078-0432.CCR-10-0434. PubMed PMID: 20966354.
47. Li J, Choi E, Yu H, Bai XC. Structural basis of the activation of type 1 insulin-like growth factor receptor. Nat Commun. 2019;10(1):4567. Epub 20191008. doi: 10.1038/s41467-019-12564-0. PubMed PMID: 31594955; PubMed Central PMCID: PMCPMC6783537.
48. Shah OJ, Hunter T. Turnover of the active fraction of IRS1 involves raptor-mTOR- and S6K1-dependent serine phosphorylation in cell culture models of tuberous sclerosis. Mol Cell Biol. 2006;26(17):6425-34. doi: 10.1128/MCB.01254-05. PubMed PMID: 16914728; PubMed Central PMCID: PMCPMC1592824.
49. Rena G, Prescott AR, Guo S, Cohen P, Unterman TG. Roles of the forkhead in rhabdomyosarcoma (FKHR) phosphorylation sites in regulating 14-3-3 binding, transactivation and nuclear targetting. Biochem J. 2001;354(Pt 3):605-12. doi: 10.1042/0264-6021:3540605. PubMed PMID: 11237865; PubMed Central PMCID: PMCPMC1221692.
50. Li A, Walling J, Kotliarov Y, Center A, Steed ME, Ahn SJ, et al. Genomic changes and gene expression profiles reveal that established glioma cell lines are poorly representative of primary human gliomas. Mol Cancer Res. 2008;6(1):21-30. PubMed PMID: 18184972.
51. Mighell TL, Evans-Dutson S, O'Roak BJ. A Saturation Mutagenesis Approach to Understanding PTEN Lipid Phosphatase Activity and Genotype-Phenotype Relationships. Am J Hum Genet. 2018;102(5):943-55. Epub 20180426. doi: 10.1016/j.ajhg.2018.03.018. PubMed PMID: 29706350; PubMed Central PMCID: PMCPMC5986715.
52. Vazquez F, Ramaswamy S, Nakamura N, Sellers WR. Phosphorylation of the PTEN tail regulates protein stability and function. Mol Cell Biol. 2000;20(14):5010-8. doi: 10.1128/MCB.20.14.5010-5018.2000. PubMed PMID: 10866658; PubMed Central PMCID: PMCPMC85951.
53. Rubio-Camacho M, Encinar JA, Martinez-Tome MJ, Esquembre R, Mateo CR. The Interaction of Temozolomide with Blood Components Suggests the Potential Use of Human Serum Albumin as a Biomimetic Carrier for the Drug. Biomolecules. 2020;10(7). Epub 20200709. doi: 10.3390/biom10071015. PubMed PMID: 32659914; PubMed Central PMCID: PMCPMC7408562.
54. Manem VS, Lambie M, Smith I, Smirnov P, Kofia V, Freeman M, et al. Modeling Cellular Response in Large-Scale Radiogenomic Databases to Advance Precision Radiotherapy. Cancer Res. 2019;79(24):6227-37. Epub 2019/09/29. doi: 10.1158/0008-5472.CAN-19-0179. PubMed PMID: 31558563; PubMed Central PMCID: PMCPMC8128135.

55. Fischer M. Census and evaluation of p53 target genes. Oncogene. 2017;36(28):3943-56. Epub 20170313. doi: 10.1038/onc.2016.502. PubMed PMID: 28288132; PubMed Central PMCID: PMCPMC5511239.
56. Villa GR, Hulce JJ, Zanca C, Bi J, Ikegami S, Cahill GL, et al. An LXR-Cholesterol Axis Creates a Metabolic Co-Dependency for Brain Cancers. Cancer cell. 2016;30(5):683-93. Epub 20161013. doi: 10.1016/j.ccell.2016.09.008. PubMed PMID: 27746144; PubMed Central PMCID: PMCPMC5479636.
57. Gimple RC, Kidwell RL, Kim LJY, Sun T, Gromovsky AD, Wu Q, et al. Glioma Stem Cell-Specific Superenhancer Promotes Polyunsaturated Fatty-Acid Synthesis to Support EGFR Signaling. Cancer discovery. 2019;9(9):1248-67. Epub 20190614. doi: 10.1158/2159-8290.CD-19-0061. PubMed PMID: 31201181; PubMed Central PMCID: PMCPMC6785242.
58. Sancho P, Barneda D, Heeschen C. Hallmarks of cancer stem cell metabolism. Br J Cancer. 2016;114(12):1305-12. Epub 20160524. doi: 10.1038/bjc.2016.152. PubMed PMID: 27219018; PubMed Central PMCID: PMCPMC4984474.
59. Yamatani Y, Nakai K. Comprehensive comparison of gene expression diversity among a variety of human stem cells. NAR Genom Bioinform. 2022;4(4):lqac087. Epub 20221129. doi: 10.1093/nargab/lqac087. PubMed PMID: 36458020; PubMed Central PMCID: PMCPMC9706419.
60. Bodzioch M, Lapicka-Bodzioch K, Zapala B, Kamysz W, Kiec-Wilk B, Dembinska-Kiec A. Evidence for potential functionality of nuclearly-encoded humanin isoforms. Genomics. 2009;94(4):247-56. Epub 20090527. doi: 10.1016/j.ygeno.2009.05.006. PubMed PMID: 19477263.
61. Wiese S, Karus M, Faissner A. Astrocytes as a source for extracellular matrix molecules and cytokines. Frontiers in pharmacology. 2012;3:120. Epub 20120626. doi: 10.3389/fphar.2012.00120. PubMed PMID: 22740833; PubMed Central PMCID: PMCPMC3382726.
62. Bochukova EG, Lawler K, Croizier S, Keogh JM, Patel N, Strohbehn G, et al. A Transcriptomic Signature of the Hypothalamic Response to Fasting and BDNF Deficiency in Prader-Willi Syndrome. Cell reports. 2018;22(13):3401-8. doi: 10.1016/j.celrep.2018.03.018. PubMed PMID: 29590610; PubMed Central PMCID: PMCPMC5896230.
63. Weichselbaum RR, Ishwaran H, Yoon T, Nuyten DS, Baker SW, Khodarev N, et al. An interferon-related gene signature for DNA damage resistance is a predictive marker for chemotherapy and radiation for breast cancer. Proc Natl Acad Sci U S A. 2008;105(47):18490-5. Epub 20081110. doi: 10.1073/pnas.0809242105. PubMed PMID: 19001271; PubMed Central PMCID: PMCPMC2587578.
64. Tanner SM, Austin JL, Leone G, Rush LJ, Plass C, Heinonen K, et al. BAALC, the human member of a novel mammalian neuroectoderm gene lineage, is implicated in hematopoiesis and acute leukemia. Proc Natl Acad Sci U S A. 2001;98(24):13901-6. Epub 2001/11/15. doi: 10.1073/pnas.241525498. PubMed PMID: 11707601; PubMed Central PMCID: PMC61139.
65. Ferrandez E, Gutierrez O, Segundo DS, Fernandez-Luna JL. NFkappaB activation in differentiating glioblastoma stem-like cells is promoted by hyaluronic acid signaling through TLR4. Sci Rep. 2018;8(1):6341. Epub 20180420. doi: 10.1038/s41598-018-24444-6. PubMed PMID: 29679017; PubMed Central PMCID: PMCPMC5910430.
66. Amsden H, Kourko O, Roth M, Gee K. Antiviral Activities of Interleukin-27: A Partner for Interferons? Front Immunol. 2022;13:902853. Epub 20220510. doi: 10.3389/fimmu.2022.902853. PubMed PMID: 35634328; PubMed Central PMCID: PMCPMC9134790.
67. Cerami E, Gao J, Dogrusoz U, Gross BE, Sumer SO, Aksoy BA, et al. The cBio cancer genomics portal: an open platform for exploring multidimensional cancer genomics data. Cancer

discovery. 2012;2(5):401-4. Epub 2012/05/17. doi: 10.1158/2159-8290.CD-12-0095. PubMed PMID: 22588877.
68. Duarte CW, Willey CD, Zhi D, Cui X, Harris JJ, Vaughan LK, et al. Expression signature of IFN/STAT1 signaling genes predicts poor survival outcome in glioblastoma multiforme in a subtype-specific manner. PloS one. 2012;7(1):e29653. Epub 20120105. doi: 10.1371/journal.pone.0029653. PubMed PMID: 22242177; PubMed Central PMCID: PMCPMC3252343.
69. Engeland K. Cell cycle arrest through indirect transcriptional repression by p53: I have a DREAM. Cell Death Differ. 2018;25(1):114-32. Epub 20171110. doi: 10.1038/cdd.2017.172. PubMed PMID: 29125603; PubMed Central PMCID: PMCPMC5729532.
70. Baskar R, Dai J, Wenlong N, Yeo R, Yeoh KW. Biological response of cancer cells to radiation treatment. Front Mol Biosci. 2014;1:24. Epub 20141117. doi: 10.3389/fmolb.2014.00024. PubMed PMID: 25988165; PubMed Central PMCID: PMCPMC4429645.
71. Fischer M, Schade AE, Branigan TB, Muller GA, DeCaprio JA. Coordinating gene expression during the cell cycle. Trends Biochem Sci. 2022;47(12):1009-22. Epub 20220711. doi: 10.1016/j.tibs.2022.06.007. PubMed PMID: 35835684.
72. Marceau AH, Brison CM, Nerli S, Arsenault HE, McShan AC, Chen E, et al. An order-to-disorder structural switch activates the FoxM1 transcription factor. Elife. 2019;8. Epub 20190528. doi: 10.7554/eLife.46131. PubMed PMID: 31134895; PubMed Central PMCID: PMCPMC6538375.
73. Srikanth M, Kim J, Das S, Kessler JA. BMP signaling induces astrocytic differentiation of clinically derived oligodendroglioma propagating cells. Mol Cancer Res. 2014;12(2):283-94. Epub 20131122. doi: 10.1158/1541-7786.MCR-13-0349. PubMed PMID: 24269952; PubMed Central PMCID: PMCPMC4006982.
74. Zhang Y, Kwok-Shing Ng P, Kucherlapati M, Chen F, Liu Y, Tsang YH, et al. A Pan-Cancer Proteogenomic Atlas of PI3K/AKT/mTOR Pathway Alterations. Cancer cell. 2017;31(6):820-32 e3. Epub 20170518. doi: 10.1016/j.ccell.2017.04.013. PubMed PMID: 28528867; PubMed Central PMCID: PMCPMC5502825.
75. Rajan P, McKay RD. Multiple routes to astrocytic differentiation in the CNS. J Neurosci. 1998;18(10):3620-9. doi: 10.1523/JNEUROSCI.18-10-03620.1998. PubMed PMID: 9570793; PubMed Central PMCID: PMCPMC6793143.
76. Cirotti C, Contadini C, Barila D. SRC Kinase in Glioblastoma News from an Old Acquaintance. Cancers. 2020;12(6). Epub 20200612. doi: 10.3390/cancers12061558. PubMed PMID: 32545574; PubMed Central PMCID: PMCPMC7352599.
77. Irtegun S, Wood RJ, Ormsby AR, Mulhern TD, Hatters DM. Tyrosine 416 is phosphorylated in the closed, repressed conformation of c-Src. PloS one. 2013;8(7):e71035. Epub 20130726. doi: 10.1371/journal.pone.0071035. PubMed PMID: 23923048; PubMed Central PMCID: PMCPMC3724807.
78. Schneider M, Ströbele S, Nonnenmacher L, Siegelin MD, Tepper M, Stroh S, et al. A paired comparison between glioblastoma “stem cells” and differentiated cells. International journal of cancer. 2016;138(7):1709-18.
79. Hasselbach LA, Irtenkauf SM, Lemke NW, Nelson KK, Berezovsky AD, Carlton ET, et al. Optimization of High Grade Glioma Cell Culture from Surgical Specimens for Use in Clinically Relevant Animal Models and 3D Immunochemistry. J Vis Exp. 2014;83:e51088. Epub 2014/01/17. doi: 10.3791/51088. PubMed PMID: 24429465.
80. Segerman A, Niklasson M, Haglund C, Bergstrom T, Jarvius M, Xie Y, et al. Clonal Variation in Drug and Radiation Response among Glioma-Initiating Cells Is Linked to Proneural-Mesenchymal Transition. Cell reports. 2016;17(11):2994-3009. doi: 10.1016/j.celrep.2016.11.056. PubMed PMID: 27974212.

81. Zielske SP. Epigenetic DNA methylation in radiation biology: on the field or on the sidelines? J Cell Biochem. 2015;116(2):212-7. doi: 10.1002/jcb.24959. PubMed PMID: 25186310.
82. Bao S, Wu Q, McLendon RE, Hao Y, Shi Q, Hjelmeland AB, et al. Glioma stem cells promote radioresistance by preferential activation of the DNA damage response. Nature. 2006;444(7120):756-60. Epub 2006/10/20. doi: 10.1038/nature05236. PubMed PMID: 17051156.
83. Hanel W, Marchenko N, Xu S, Xiaofeng Yu S, Weng W, Moll U. Two hot spot mutant p53 mouse models display differential gain of function in tumorigenesis. Cell Death & Differentiation. 2013;20(7):898-909.
84. Cheon H, Wang Y, Wightman SM, Jackson MW, Stark GR. How cancer cells make and respond to interferon-I. Trends in cancer. 2023;9(1):83-92.
85. Widau RC, Parekh AD, Ranck MC, Golden DW, Kumar KA, Sood RF, et al. RIG-I–like receptor LGP2 protects tumor cells from ionizing radiation. Proceedings of the National Academy of Sciences. 2014;111(4):E484-E91.
86. Leonova KI, Brodsky L, Lipchick B, Pal M, Novototskaya L, Chenchik AA, et al. p53 cooperates with DNA methylation and a suicidal interferon response to maintain epigenetic silencing of repeats and noncoding RNAs. Proceedings of the National Academy of Sciences. 2013;110(1):E89-E98.
87. Khodarev NN, Beckett M, Labay E, Darga T, Roizman B, Weichselbaum RR. STAT1 is overexpressed in tumors selected for radioresistance and confers protection from radiation in transduced sensitive cells. Proceedings of the National Academy of Sciences. 2004;101(6):1714-9.
88. Kondratova A, Cheon H, Dong B, Holvey-Bates EG, Hasipek M, Taran I, et al. Suppressing PARylation by 2',5'-oligoadenylate synthetase 1 inhibits DNA damage-induced cell death. EMBO J. 2020;39(20):e106593. doi: 10.15252/embj.2020106593. PubMed PMID: 33058249; PubMed Central PMCID: PMCPMC7560197.
89. Miranda A, Hamilton PT, Zhang AW, Pattnaik S, Becht E, Mezheyeuski A, et al. Cancer stemness, intratumoral heterogeneity, and immune response across cancers. Proc Natl Acad Sci U S A. 2019;116(18):9020-9. Epub 20190417. doi: 10.1073/pnas.1818210116. PubMed PMID: 30996127; PubMed Central PMCID: PMCPMC6500180.
90. Zhan X, Guo S, Li Y, Ran H, Huang H, Mi L, et al. Glioma stem-like cells evade interferon suppression through MBD3/NuRD complex–mediated STAT1 downregulation. Journal of Experimental Medicine. 2020;217(5):e20191340.
91. Senut MC, Sen A, Cingolani P, Shaik A, Land SJ, Ruden DM. Lead exposure disrupts global DNA methylation in human embryonic stem cells and alters their neuronal differentiation. Toxicol Sci. 2014;139(1):142-61. Epub 2014/02/13. doi: 10.1093/toxsci/kfu028. PubMed PMID: 24519525; PubMed Central PMCID: PMCPMC4023291.
92. Haidet-Phillips AM, Hester ME, Miranda CJ, Meyer K, Braun L, Frakes A, et al. Astrocytes from familial and sporadic ALS patients are toxic to motor neurons. Nat Biotechnol. 2011;29(9):824-8. Epub 2011/08/13. doi: 10.1038/nbt.1957. PubMed PMID: 21832997; PubMed Central PMCID: PMCPMC3170425.
93. Gu Z, Eils R, Schlesner M. Complex heatmaps reveal patterns and correlations in multidimensional genomic data. Bioinformatics. 2016;32(18):2847-9. Epub 20160520. doi: 10.1093/bioinformatics/btw313. PubMed PMID: 27207943.
94. Irtenkauf SM, Sobiechowski S, Hasselbach LA, Nelson KK, Transou AD, Carlton ET, et al. Optimization of Glioblastoma Mouse Orthotopic Xenograft Models for Translational Research. Comparative medicine. 2017;67(4):300-14. Epub May 16. doi: no_doi/1494959945479. PubMed PMID: 28830577; PubMed Central PMCID: PMCPMC5557202.

95. Andrews S. FastQC A Quality Control Tool for High Throughput Sequence Data. Available online at: http://www.bioinformatics.babraham.ac.uk/projects/fastqc2010.
96. Kim D, Pertea G, Trapnell C, Pimentel H, Kelley R, Salzberg SL. TopHat2: accurate alignment of transcriptomes in the presence of insertions, deletions and gene fusions. Genome Biol. 2013;14(4):R36. Epub 2013/04/27. doi: 10.1186/gb-2013-14-4-r36. PubMed PMID: 23618408; PubMed Central PMCID: PMCPMC4053844.
97. Trapnell C, Pachter L, Salzberg SL. TopHat: discovering splice junctions with RNA-Seq. Bioinformatics. 2009;25(9):1105-11. Epub 2009/03/18. doi: 10.1093/bioinformatics/btp120. PubMed PMID: 19289445; PubMed Central PMCID: PMCPMC2672628.
98. Li H, Handsaker B, Wysoker A, Fennell T, Ruan J, Homer N, et al. The Sequence Alignment/Map format and SAMtools. Bioinformatics. 2009;25(16):2078-9. Epub 2009/06/10. doi: 10.1093/bioinformatics/btp352. PubMed PMID: 19505943; PubMed Central PMCID: PMCPMC2723002.
99. Tarazona S, Furio-Tari P, Turra D, Pietro AD, Nueda MJ, Ferrer A, et al. Data quality aware analysis of differential expression in RNA-seq with NOISeq R/Bioc package. Nucleic acids research. 2015;43(21):e140. Epub 2015/07/18. doi: 10.1093/nar/gkv711. PubMed PMID: 26184878; PubMed Central PMCID: PMCPMC4666377.
100. Zhou Y, Zhou B, Pache L, Chang M, Khodabakhshi AH, Tanaseichuk O, et al. Metascape provides a biologist-oriented resource for the analysis of systems-level datasets. Nat Commun. 2019;10(1):1523. Epub 2019/04/05. doi: 10.1038/s41467-019-09234-6. PubMed PMID: 30944313; PubMed Central PMCID: PMCPMC6447622.
101. Davis S, Du P, Bilke S, Triche Jr. T, Bootwalla M. methylumi: Handle Illumina methylation data. R package version 2.30.0. (DOI: 10.18129/B9.bioc.methylumi). 2019.
102. Zhou W, Laird PW, Shen H. Comprehensive characterization, annotation and innovative use of Infinium DNA methylation BeadChip probes. Nucleic acids research. 2017;45(4):e22. Epub 2016/12/08. doi: 10.1093/nar/gkw967. PubMed PMID: 27924034; PubMed Central PMCID: PMCPMC5389466.
103. Leek JT, Johnson WE, Parker HS, Fertig EJ, Jaffe AE, Storey JD, et al. sva: Surrogate Variable Analysis. R package version 3.32.1. 2019.
104. Johnson WE, Li C, Rabinovic A. Adjusting batch effects in microarray expression data using empirical Bayes methods. Biostatistics (Oxford, England). 2007;8(1):118-27. Epub 2006/04/25. doi: 10.1093/biostatistics/kxj037. PubMed PMID: 16632515.
105. Hansen KD, Aryee M. IlluminaHumanMethylation450kmanifest: Annotation for Illumina's 450k methylation arrays. R package version 0.4.0. (DOI: 10.18129/B9.bioc.IlluminaHumanMethylation450kmanifest). 2012.
106. Tian Y, Morris TJ, Webster AP, Yang Z, Beck S, Feber A, et al. ChAMP: updated methylation analysis pipeline for Illumina BeadChips. Bioinformatics. 2017;33(24):3982-4. doi: 10.1093/bioinformatics/btx513. PubMed PMID: 28961746; PubMed Central PMCID: PMCPMC5860089.
107. Clough E, Barrett T, Wilhite SE, Ledoux P, Evangelista C, Kim IF, et al. NCBI GEO: archive for gene expression and epigenomics data sets: 23-year update. Nucleic acids research. 2023. Epub 20231102. doi: 10.1093/nar/gkad965. PubMed PMID: 37933855.

Supporting information

S1_Fig. Alteration in glioblastoma cancer stem cell signaling in response to growth factors withdrawal and differentiation in 2% FBS. A) Box plot representing changes in the levels of 66 proteins/PTM in response to 14-days culture in the absence of growth factors (NM), or upon serum differentiation (2%FBS), relative to CSC culture conditions (NMGF), using mean

values from triplicate RPPA measurements for each of the 8 models. Plot represents n=507 data points, after proteins/PTMs which were not detected under all three culture conditions were filtered out for each model.

S2_Fig. MGMT promoter methylation. Heatmap representing β-values of 26 CpG sites mapping to MGMT promoter, for HF2303 and HF2927 CSC and SDCs in control, TMZ and RT treatment groups, in triplicate. Human astrocyte cell line was included as reference. The two probes widely employed in the clinic to determine MGMT promoter methylation status ("predictive probes") indicate MGMT promoter hypermethylation in HF2927 and unmethylated status in HF2303 and human astrocytes cells. Differentiation status and treatment did not alter promoter methylation levels for either GBM line.

S3_Fig. Alterations in cellular respiration in response to treatment. A) Basal (B) and maximum (M) relative oxygen consumption rate (OCR) for CSCs and SDCs measured after a 4-day treatment with TMZ, or 4 days after treatment with one 4 Gy radiation dose. OCR values were normalized to CSC (left panel) and SDC (right panel) HF2303 basal levels (%). Measurements for n=2-3 repeats with means are shown. B) Reserve respiratory capacity was calculated as ratio of (mean maximum)/(mean basal) O2 consumption.

S4_Fig. Short term treatment with TMZ and RT did not significantly alter DNA methylation pattern of glioblastoma CSCs and SDCs. Principal component analysis for b-values for all treatment groups in triplicates for each cell line and differentiation status: HF2303 CSC (A), HF2303 SDCs (B), HF2927 CSCs (C), and HF2927 SDCs (D).

S1 Table. Reverse Phase Protein Array (RPPA) Targets, Values, Signaling Pathways

S2 Table. Differentially expressed gene lists

S3 Table. Interferon signaling correlation group in glioblastoma (TCGA)

S4 Table. Differentially methylated probes

FIGURES AND LEGENDS

A

Patient-derived model ID	Clinical and demographic								Molecular										
	Pathology	Treatment status at collection	Sex	Age @ diagnosis	Rx1	TTP1 (days)	OS (days)	MGMT promoter	TP53	MDM2	CDKN2A	CDK4	EGFR	MET	PTEN	NF1	MYC	Transcriptional subclass	Molecular profiling consortium ID
HF2303	GS	untreated	M	62	RT/ TMZ	88	317	U	p.G245S	0	0	0	0	0	p.D92E	p.W561R	0	Mesenchymal	TCGA-06-0190
HF2354	GBM	BCNU	M	61	RT/ TMZ	60	196	U	p.V216L	0	HOM DEL	0	0	0	splice mut	WT	AMP	ND	n/a
HF2587	GBM	untreated	F	56	RT/ TMZ	232	360	M	WT	0	HOM DEL	0	0	0	p.Q298*	p.W267*	0	Proneural	n/a
HF2927	GBM	untreated	F	55	RT/ TMZ	555	664	M	WT	0	HOM DEL	0	AMP, vIII	0	HOM DEL	WT	0	Classical	n/a
HF3016	GBM	untreated	M	45	RT/ TMZ	88	646	U	p.M133T	0	0	AMP	AMP	0	p.I122S	WT	AMP	Proneural	GLSS-HF-3016-TP
HF3035	GBM	untreated	F	54	RT/ TMZ	196	352	M	WT	0	HOM DEL	0	0	AMP	HOM DEL	WT	0	Classical	n/a
HF3055	GBM	untreated	M	58	RT/ TMZ	77	371	U	WT	AMP	0	AMP	AMP	0	HOM DEL	WT	0	Classical	n/a
HF3077	GBM	untreated	F	56	RT/ TMZ	54	465	M	p.G266E	0	HOM DEL	0	0	AMP	WT	p.R2637*	0	Proneural	n/a

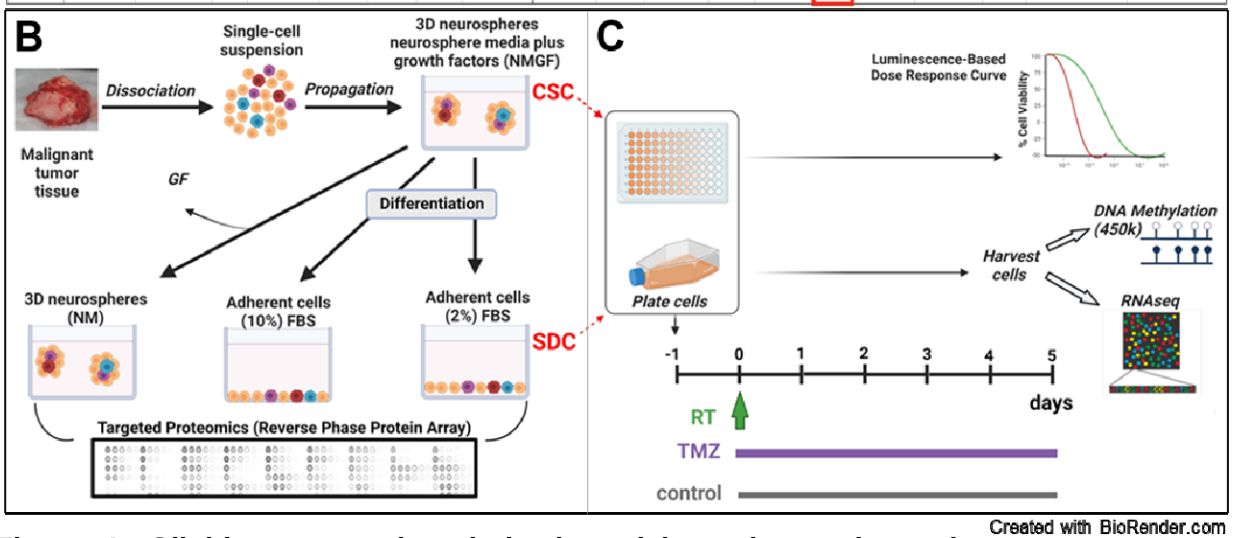

Figure 1. Glioblastoma patient-derived models and experimental design. A) Clinical and molecular data associated with the GBM patient-derived models. RT, radiation therapy; TMZ, temozolomide; Rx1, first-line therapy; TTP, time to progression; OS, overall survival; U, unmethylated; M, methylated MGMT promoter. Red outline denotes extrachromosomal (ecDNA) amplification. **B)** Schematic depicting neurosphere culture in NMGF media for selection and amplification of cancer stem cells (CSCs) from surgical specimens, followed by 2 weeks incubation in altered conditions: withdrawal of growth factors (NM), and addition of 2% and 10% FBS. For the purposes of this study, serum-differentiated cells (SDC) are those cultured in 2% FBS. The effect of the different culture conditions on cell signaling were compared by RPPA. **C)** The sensitivity of CSC and SDC for a subset of the models to single dose radiation (RT) or 5-day TMZ was measured. Transcriptional and epigenomic reprograming in SDC vs CSC, and in response to treatment were evaluated by bulk RNAseq and 450k DNA methylation array.

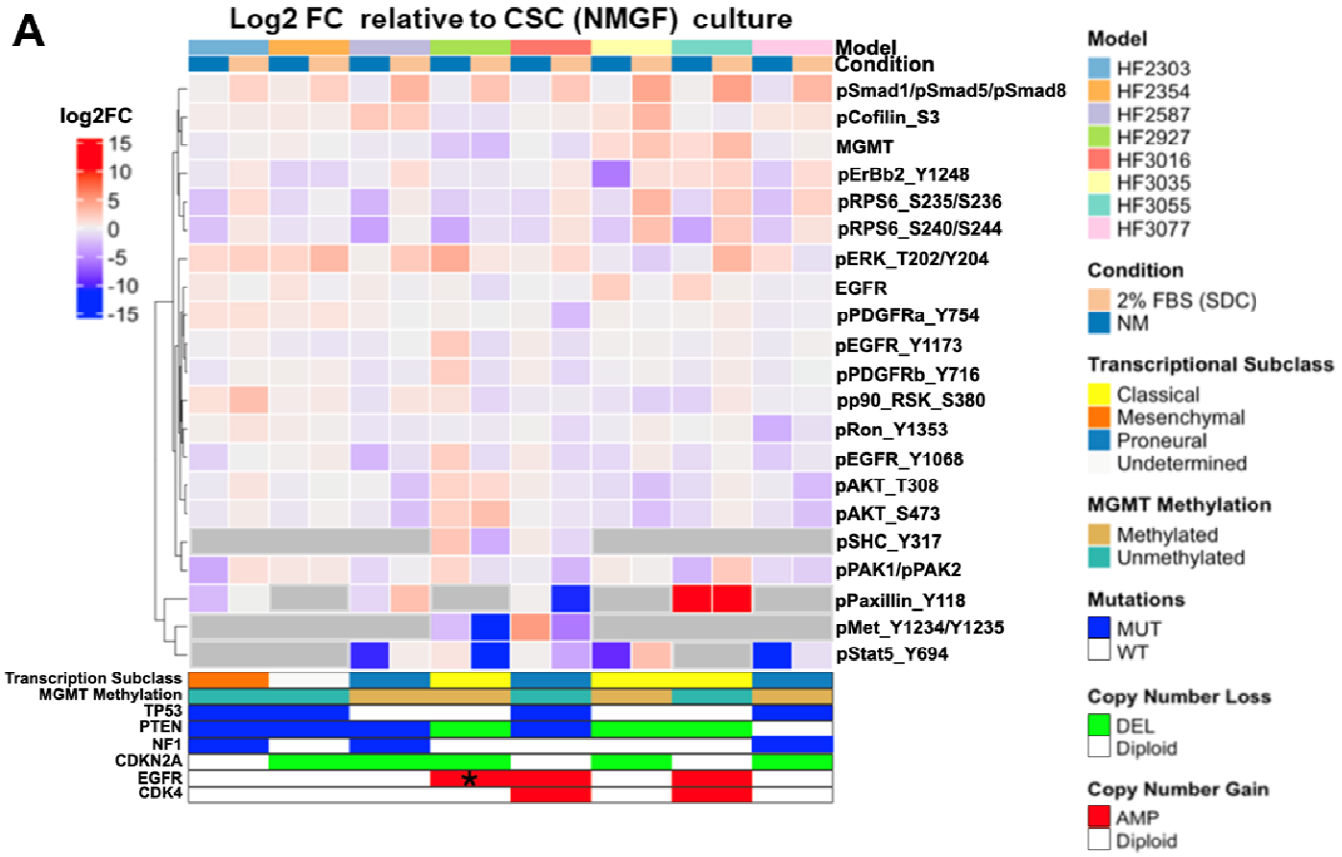

B

	pEGFR_Y1068	pPDGFRb_Y716	pSrc_Y416	pSrc_Y527	pStat3_S727	p-Smad1/5/8	pAKT_S473	pAKT_T308	pGSK3a/b_S21/S9	pmTOR_S2448	pp70_S6K_T412	pRPS6_S235/S236	pRPS6_S240/S244	pP38_T180/Y182	pp90_RSK_S380	pErk_T202/Y204	pAMPKa1_S485	pAMPKb1_S108	pIRS1_S612	pFKHR_S256
pEGFR_Y1068	1.0	0.9	0.3	0.3	0.3	-0.1	-0.2	-0.2	-0.3	0.2	-0.2	-0.2	-0.3			-0.1	0.1		-0.1	-0.2
pPDGFRb_Y716	0.9	1.0	0.3	0.3	0.3	-0.1	-0.2	-0.2	-0.3	0.2	-0.2	-0.2	-0.2		0.1	-0.1	0.1	0.1	-0.1	-0.3
pSrc_Y416	0.3	0.3	1.0	0.7	0.3	-0.1	-0.2	-0.1		0.2	0.3	0.3	0.2	0.3	0.2	0.1		0.4	-0.1	0.2
pSrc_Y527	0.3	0.3	0.7	1.0	0.1	-0.2	-0.3	-0.2		0.3		0.2	0.1		-0.1	-0.2	-0.1	0.4	-0.1	0.3
pStat3_S727	0.3	0.3	0.3	0.1	1.0	0.1	-0.3	-0.3		0.6	0.7	0.4	0.4	0.4	0.7		0.5	0.6	0.3	0.5
p-Smad1/5/8	-0.1	-0.1	-0.1	-0.2	0.1	1.0	-0.4	-0.4	-0.4		0.1	0.5	0.5	0.3	-0.2	0.1	-0.1	0.1	0.3	
pAKT_S473	-0.2	-0.2	-0.2	-0.3	-0.3	-0.4	1.0	1.0	0.8	-0.1	0.1	-0.2	-0.1		0.2	0.5	0.4	-0.2	0.1	
pAKT_T308	-0.2	-0.2	-0.1	-0.2	-0.3	-0.4	1.0	1.0	0.8	-0.1	0.1	-0.2	-0.1		0.1	0.6	0.4	-0.2	0.1	
pGSK3a/b_S21/S9	-0.3	-0.3				-0.4	0.8	0.8	1.0	0.2	0.3	0.1	0.2		0.4	0.5	0.6	0.1	0.4	0.4
pmTOR_S2448	0.2	0.2	0.2	0.3	0.6		-0.1	-0.1	0.2	1.0	0.6	0.6	0.6	0.4	0.4	-0.2	0.4	0.9	0.1	0.5
pp70_S6K_T412	-0.2	-0.2	0.3		0.7	0.1	0.1	0.1	0.3	0.6	1.0	0.7	0.7	0.6	0.6	0.1	0.5	0.6	0.2	0.5
pRPS6_S235/S236	-0.2	-0.2	0.3	0.2	0.4	0.5	-0.2	-0.2	0.1	0.6	0.7	1.0	1.0	0.5	0.2	-0.1	0.2	0.6	0.3	0.5
pRPS6_S240/S244	-0.3	-0.2	0.2	0.1	0.4	0.5	-0.1	-0.1	0.2	0.6	0.7	1.0	1.0	0.4	0.2	-0.1	0.3	0.6	0.4	0.6
pP38_T180/Y182			0.3		0.4	0.3				0.4	0.6	0.5	0.4	1.0	0.4	0.3	0.2	0.5	0.1	0.1
pp90_RSK_S380		0.1	0.2	-0.1	0.7	-0.2	0.2	0.1	0.4	0.4	0.6	0.2	0.2	0.4	1.0	0.3	0.7	0.5	0.4	0.6
pErk_T202/Y204	-0.1	-0.1	0.1	-0.2		0.1	0.5	0.6	0.5	-0.2	0.1	-0.1	-0.1	0.3	0.3	1.0	0.4	-0.1	0.3	0.1
pAMPKa1_S485	0.1	0.1		-0.1	0.5	-0.1	0.4	0.4	0.6	0.4	0.5	0.2	0.3	0.2	0.7	0.4	1.0	0.3	0.5	0.5
pAMPKb1_S108		0.1	0.4	0.4	0.6	0.1	-0.2	-0.2	0.1	0.9	0.6	0.6	0.6	0.5	0.5	-0.1	0.3	1.0	0.1	0.6
pIRS1_S612	-0.1	-0.1	-0.1	-0.1	0.3	0.3	0.1	0.1	0.4	0.1	0.2	0.3	0.4	0.1	0.4	0.3	0.5	0.1	1.0	0.6
pFKHR_S256	-0.2	-0.3	0.2	0.3	0.5				0.4	0.5	0.5	0.5	0.6	0.1	0.6	0.1	0.5	0.6	0.6	1.0

Spearman correlation coefficient (r)

1.0
0.5
0
-0.5
-1.0

Figure 2. Targeted proteomics reveals common and cell specific alterations in key signaling CSCs in response to differentiation and identifies interdependencies in activation of key signaling mediators. A) Heatmap depicting log2FC relative to NMGF (CSC) for the top 5% most variable proteins/PTM. Each value represents mean log2FC for n=3 RPPA measurements/group. proteins/PTMs which were not detected under all three culture conditions were filtered out for each model (grey cells). **B)** Heatmap of Spearman correlation coefficient values comparing phosphorylation levels in key cell signaling mediators in 8 patient derived GBM models grown in 4 media conditions in triplicates.

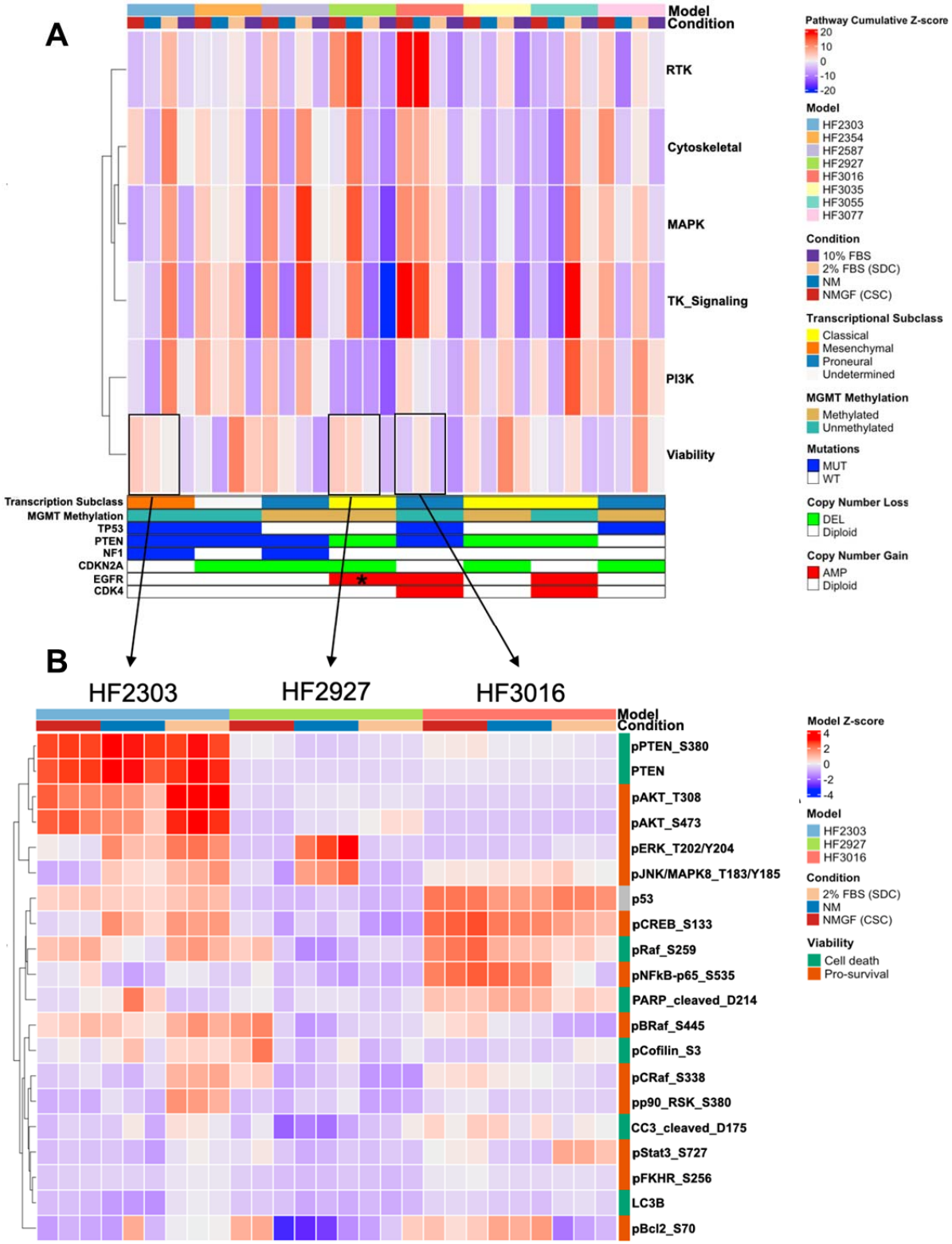

Figure 3. Comparative targeted proteomics of CSCs growing in 4 different conditions. A) Heatmap depicting mean signaling pathway activation for triplicate samples in 4 culture

conditions, for CSCs derived from 8 patients with diverse genomic landscape, transcriptional subclass and MGMT promoter methylation. Hierarchical clustering of rows was based on Spearman correlation analysis. **B)** Heatmap for protein/PTM z-scores involved in cell death and survival signaling for 3 models grown in NMGF (CSC), NM and 2% FBS (SDC), in triplicate (boxes in (A)).

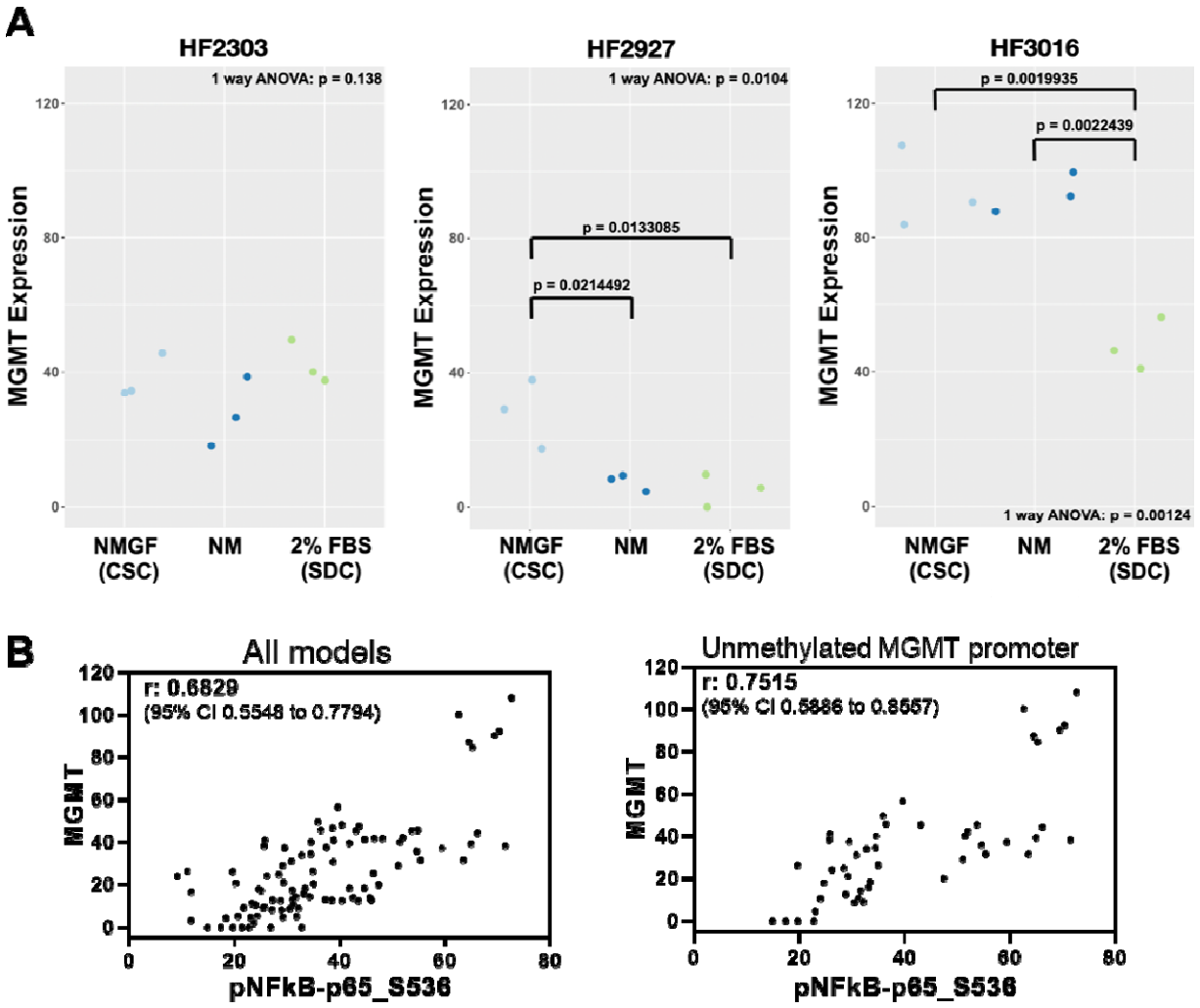

Figure 4. The impact of culture conditions on MGMT protein expression is cell line specific and correlates with NFkB activation. A) MGMT protein levels measure by RPPA for the same samples described in (B). P-values for 1-way ANOVA and post-hoc TukeyHSD test for comparison of the effect of culture conditions on MGMT protein expression are shown. **B)** Correlation of the levels of MGMT and phospho-NFkB (S536), for all 8 GBM models and culture conditions (left panel) and for the 4 models presenting unmethylated MGMT promoter (right panel). Spearman r and 95% CI are shown.

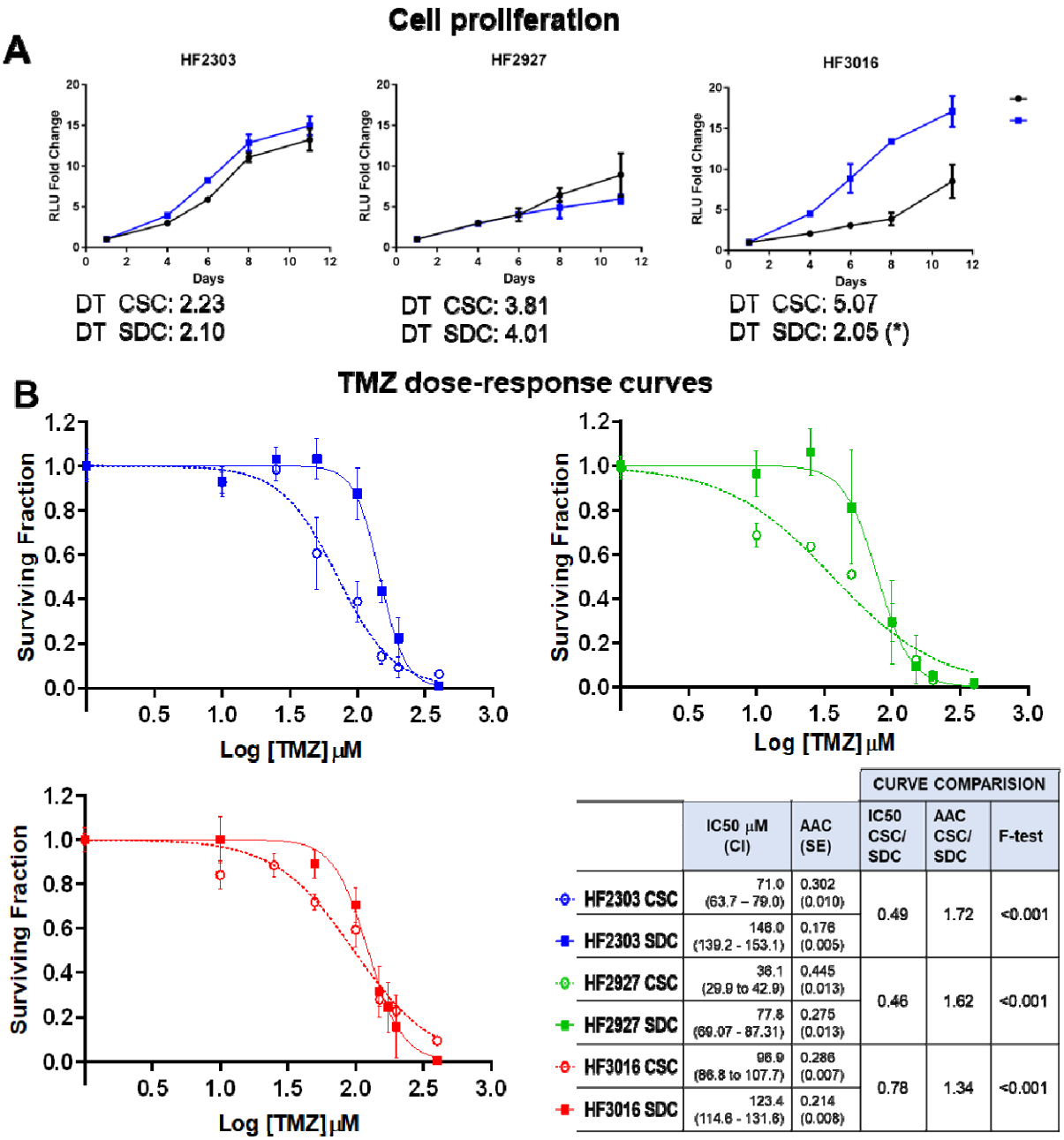

	IC50 µM (CI)	AAC (SE)	CURVE COMPARISION IC50 CSC/ SDC	AAC CSC/ SDC	F-test
HF2303 CSC	71.0 (63.7 – 79.0)	0.302 (0.010)	0.49	1.72	<0.001
HF2303 SDC	146.0 (139.2 - 153.1)	0.176 (0.005)			
HF2927 CSC	36.1 (29.9 to 42.9)	0.445 (0.013)	0.46	1.62	<0.001
HF2927 SDC	77.8 (69.07 - 87.31)	0.275 (0.013)			
HF3016 CSC	96.9 (86.8 to 107.7)	0.286 (0.007)	0.78	1.34	<0.001
HF3016 SDC	123.4 (114.6 - 131.6)	0.214 (0.008)			

Figure 5. **GBM CSCs are more sensitive to temozolomide than SDCs. A)** To compare cell proliferation rates, CSCs and SDCs for each line were plated in the respective media in 96-well assay plates (1,000 cells/well) and cell viability was measured over 11 days in culture (n=5). Graphs represent mean (SE). The calculated doubling-times (DT, days) are shown, pairwise comparison between CSC and SDC values were significant for HF3016 only (*) p<0.01. **B)** Cells were plated in 96-well assay plates (2,000/plate) and treated for 5 days with the indicated doses

of temozolomide, or equivalent DMSO control. Dose-response curves, the calculated IC50 concentrations with confidence interval (CI), and area above the curve (AAC) expressed as a fraction of total area with SE are shown. For each of the GBM patients, CSCs were significantly more sensitive to TMZ relative to SDCs, as shown by IC50 and AAC ratios, and p-values for dose-response curve comparison (F-test).

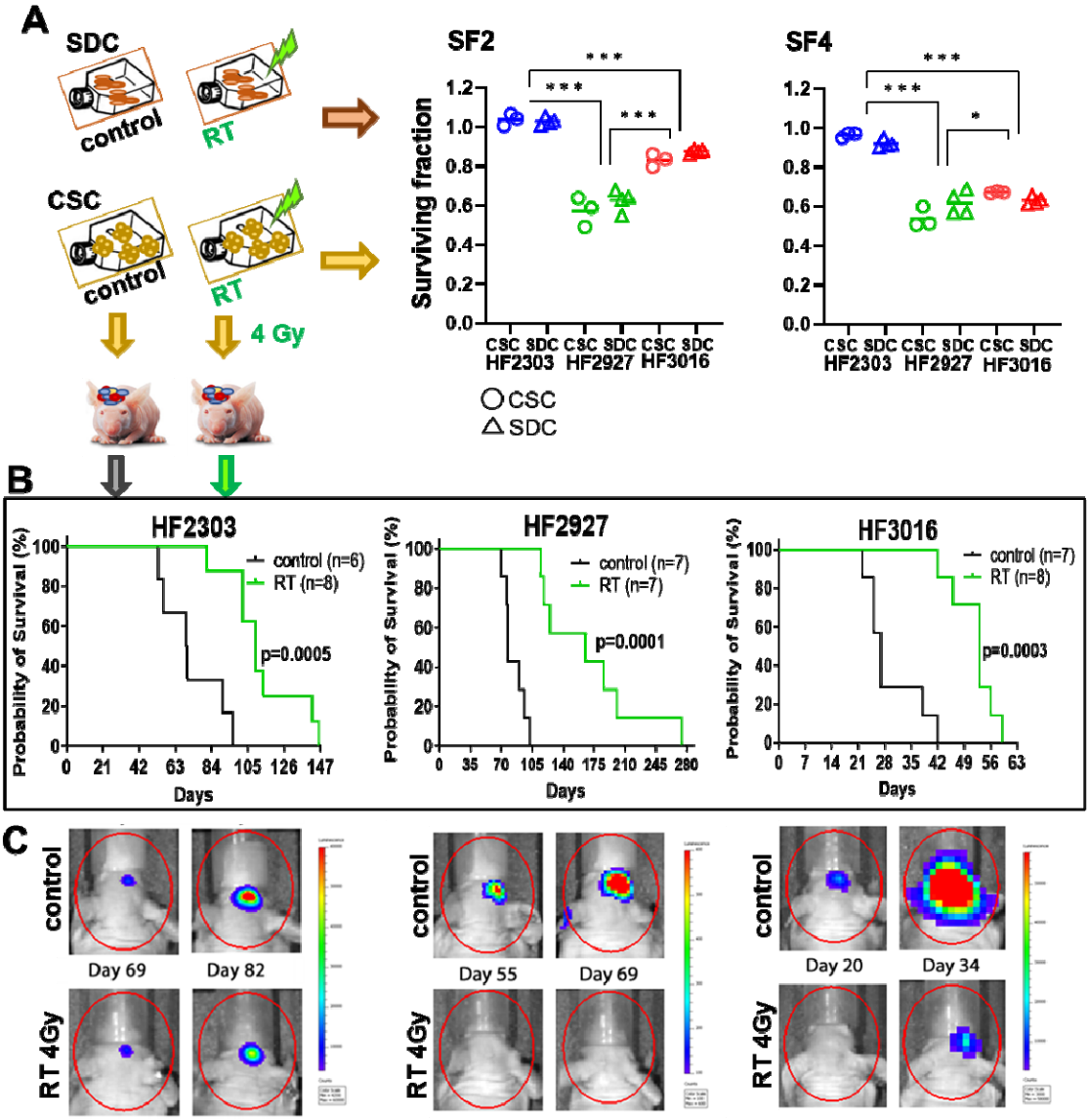

Figure 6. **Response of glioblastoma CSCs and SDCs to ionizing radiation**. **A)** CSC and SDC received a single radiation dose (2Gy or 4Gy) or mock radiation (control), and cell viability was measured 5 days later (n=3-4). No significant difference in sensitivity to RT between CSC and SDCs was observed for any of the lines (Holm-Sidak multiple comparisons test with adj p-value<0.05 threshold). The SF values among the 3 cell lines (CSC and SDC combined) were compared by one-way ANOVA, followed by Tukey's multiple comparisons tests, adj p value<0.0001(***), <0.05 (*). **B)** Irradiated and control CSCs were implanted intracranially immediately after treatment, 3x10^5 cells/mouse (n=6-8/group). Symptom-free survival for the

orthotopic PDX is shown in Kaplan-Meier curves, compared by log-rank test. **C)** Longitudinal live bioluminescense images for representative PDX in (B).

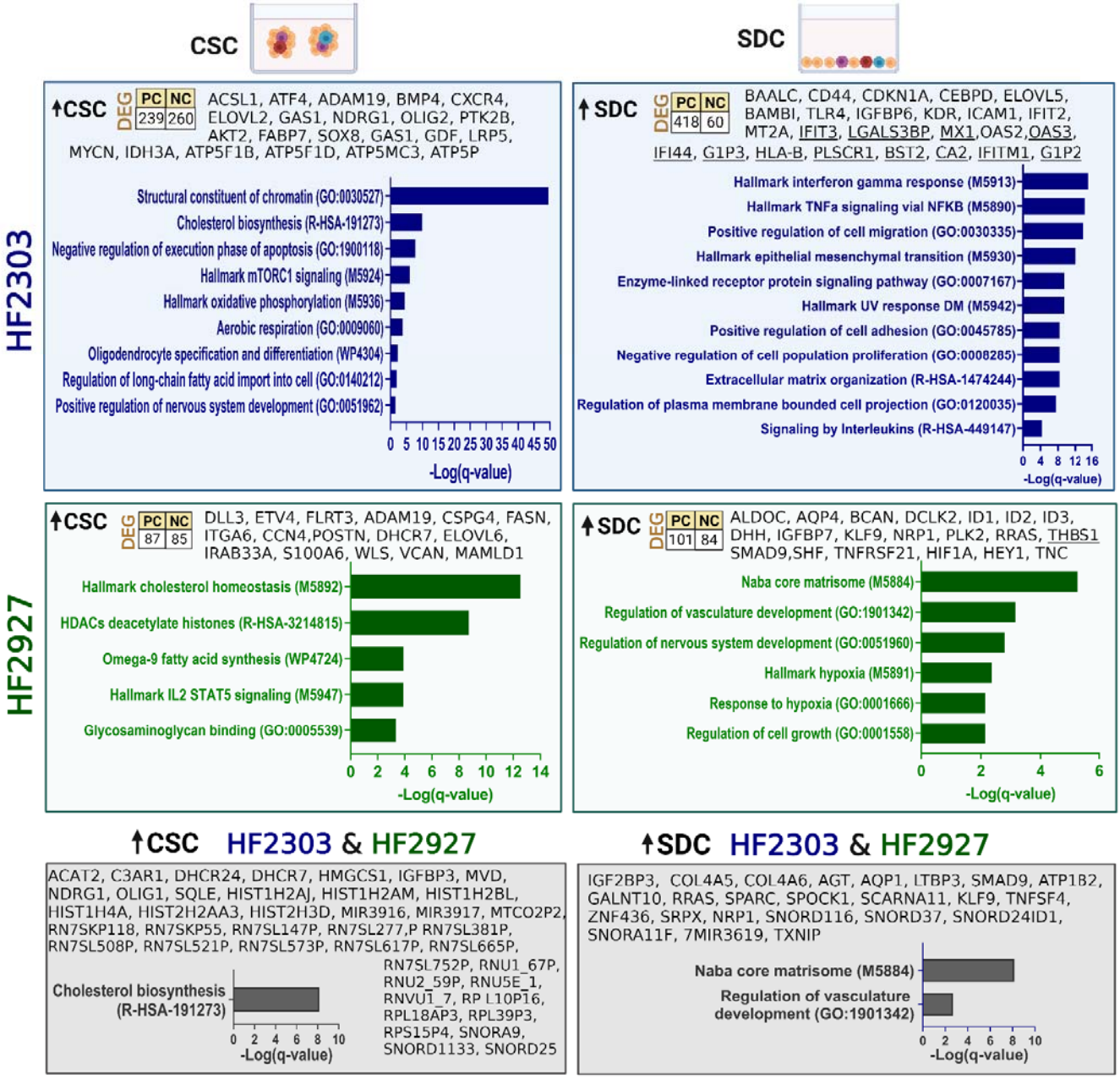

Figure 7: Transcriptional reprograming in glioblastoma cells in response to CSC differentiation. HF2927 and HF2303 CSC were grown in regular neurosphere media or in SDC cultures for 2 weeks. Total RNA from triplicate samples for each group was sequenced analyzed and DEG between CSC and SDC determined for each line. Total number of upregulated and downregulated protein coding (PC) and non-coding (NC) genes. Select genes from each list are shown. Metascape gene-set enrichment tests were adjusted for multiple

comparisons, pathways with q-value < 0.05 are shown. The 43 genes upregulated in CSCs and the 25 genes upregulated in SDCs for both cell lines, along with enriched cellular processes are shown in the grey boxes.

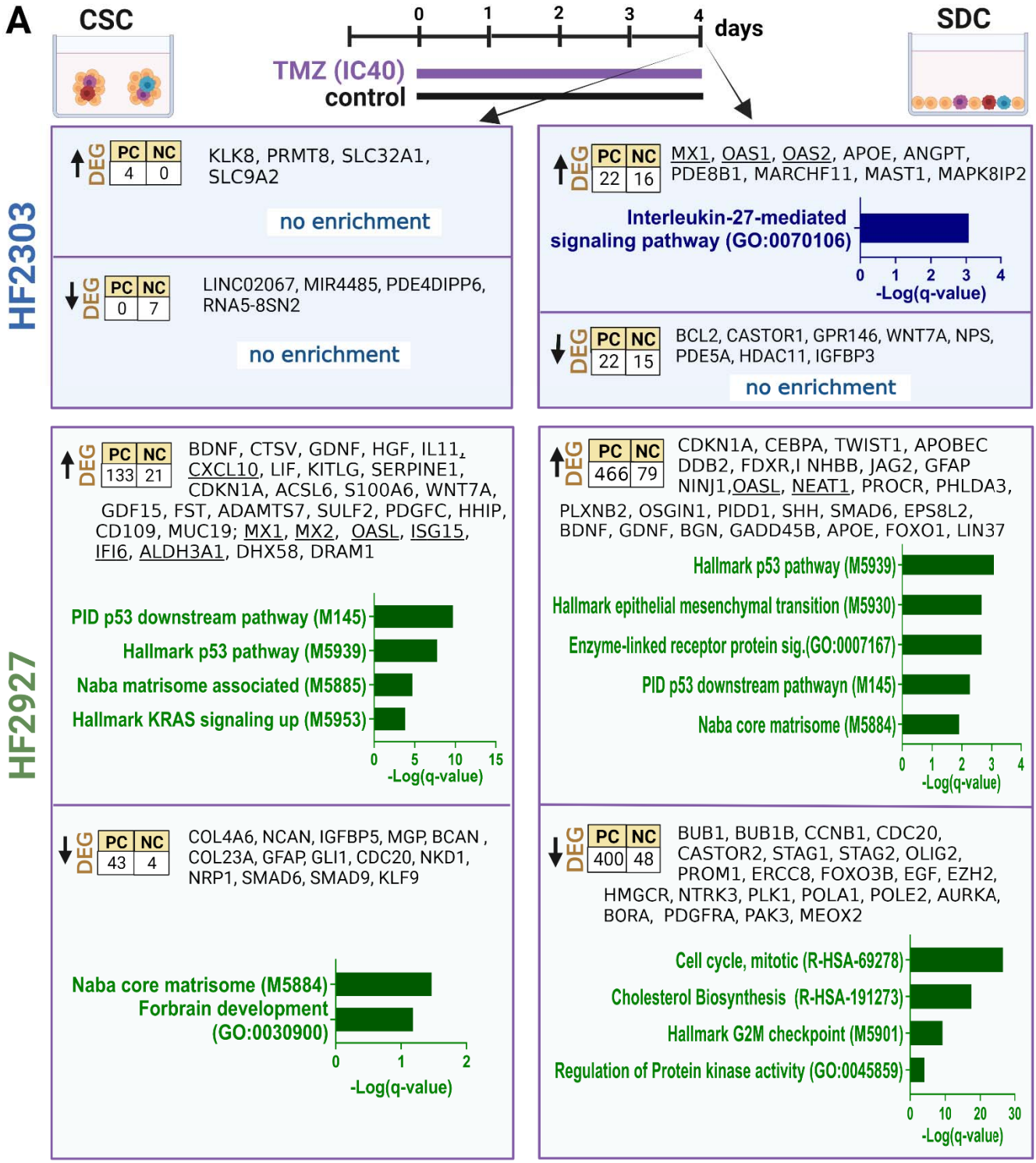
A
CSC
SDC
0
1
2
3
4
days
TMZ (IC40)
control
HF2303
HF2927
DEG
PC NC
4 0
KLK8, PRMT8, SLC32A1, SLC9A2
no enrichment
DEG
PC NC
0 7
LINC02067, MIR4485, PDE4DIPP6, RNA5-8SN2
no enrichment
DEG
PC NC
22 16
MX1, OAS1, OAS2, APOE, ANGPT, PDE8B1, MARCHF11, MAST1, MAPK8IP2
Interleukin-27-mediated signaling pathway (GO:0070106)
0 1 2 3 4
-Log(q-value)
DEG
PC NC
22 15
BCL2, CASTOR1, GPR146, WNT7A, NPS, PDE5A, HDAC11, IGFBP3
no enrichment
DEG
PC NC
133 21
BDNF, CTSV, GDNF, HGF, IL11, CXCL10, LIF, KITLG, SERPINE1, CDKN1A, ACSL6, S100A6, WNT7A, GDF15, FST, ADAMTS7, SULF2, PDGFC, HHIP, CD109, MUC19; MX1, MX2, OASL, ISG15, IFI6, ALDH3A1, DHX58, DRAM1
PID p53 downstream pathway (M145)
Hallmark p53 pathway (M5939)
Naba matrisome associated (M5885)
Hallmark KRAS signaling up (M5953)
0 5 10 15
-Log(q-value)
DEG
PC NC
466 79
CDKN1A, CEBPA, TWIST1, APOBEC DDB2, FDXR,I NHBB, JAG2, GFAP NINJ1,OASL, NEAT1, PROCR, PHLDA3, PLXNB2, OSGIN1, PIDD1, SHH, SMAD6, EPS8L2, BDNF, GDNF, BGN, GADD45B, APOE, FOXO1, LIN37
Hallmark p53 pathway (M5939)
Hallmark epithelial mesenchymal transition (M5930)
Enzyme-linked receptor protein sig.(GO:0007167)
PID p53 downstream pathwayn (M145)
Naba core matrisome (M5884)
0 1 2 3 4
-Log(q-value)
DEG
PC NC
43 4
COL4A6, NCAN, IGFBP5, MGP, BCAN , COL23A, GFAP, GLI1, CDC20, NKD1, NRP1, SMAD6, SMAD9, KLF9
Naba core matrisome (M5884)
Forbrain development (GO:0030900)
0 1 2
-Log(q-value)
DEG
PC NC
400 48
BUB1, BUB1B, CCNB1, CDC20, CASTOR2, STAG1, STAG2, OLIG2, PROM1, ERCC8, FOXO3B, EGF, EZH2, HMGCR, NTRK3, PLK1, POLA1, POLE2, AURKA, BORA, PDGFRA, PAK3, MEOX2
Cell cycle, mitotic (R-HSA-69278)
Cholesterol Biosynthesis (R-HSA-191273)
Hallmark G2M checkpoint (M5901)
Regulation of Protein kinase activity (GO:0045859)
0 10 20 30
-Log(q-value)

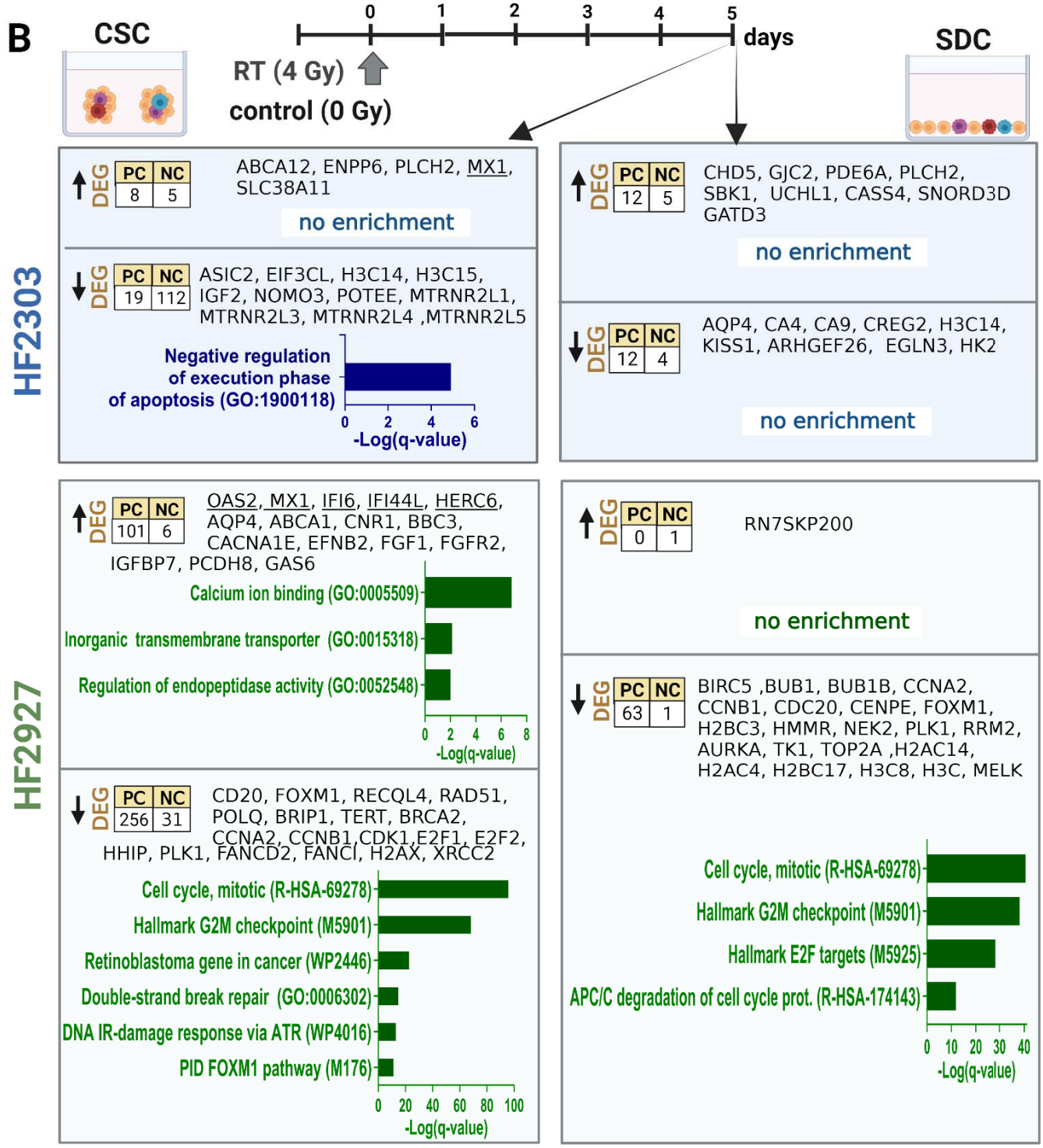
B
CSC
0
1
2
3
4
5
days
SDC
RT (4 Gy)
control (0 Gy)
HF2303
DEG
PC NC
8 5
ABCA12, ENPP6, PLCH2, MX1, SLC38A11
no enrichment
DEG
PC NC
19 112
ASIC2, EIF3CL, H3C14, H3C15, IGF2, NOMO3, POTEE, MTRNR2L1, MTRNR2L3, MTRNR2L4 ,MTRNR2L5
Negative regulation of execution phase of apoptosis (GO:1900118)
0 2 4 6
-Log(q-value)
DEG
PC NC
12 5
CHD5, GJC2, PDE6A, PLCH2, SBK1, UCHL1, CASS4, SNORD3D GATD3
no enrichment
DEG
PC NC
12 4
AQP4, CA4, CA9, CREG2, H3C14, KISS1, ARHGEF26, EGLN3, HK2
no enrichment
HF2927
DEG
PC NC
101 6
OAS2, MX1, IFI6, IFI44L, HERC6, AQP4, ABCA1, CNR1, BBC3, CACNA1E, EFNB2, FGF1, FGFR2, IGFBP7, PCDH8, GAS6
Calcium ion binding (GO:0005509)
Inorganic transmembrane transporter (GO:0015318)
Regulation of endopeptidase activity (GO:0052548)
0 2 4 6 8
-Log(q-value)
DEG
PC NC
256 31
CD20, FOXM1, RECQL4, RAD51, POLQ, BRIP1, TERT, BRCA2, CCNA2, CCNB1,CDK1,E2F1, E2F2, HHIP, PLK1, FANCD2, FANCI, H2AX, XRCC2
Cell cycle, mitotic (R-HSA-69278)
Hallmark G2M checkpoint (M5901)
Retinoblastoma gene in cancer (WP2446)
Double-strand break repair (GO:0006302)
DNA IR-damage response via ATR (WP4016)
PID FOXM1 pathway (M176)
0 20 40 60 80 100
-Log(q-value)
DEG
PC NC
0 1
RN7SKP200
no enrichment
DEG
PC NC
63 1
BIRC5 ,BUB1, BUB1B, CCNA2, CCNB1, CDC20, CENPE, FOXM1, H2BC3, HMMR, NEK2, PLK1, RRM2, AURKA, TK1, TOP2A ,H2AC14, H2AC4, H2BC17, H3C8, H3C, MELK
Cell cycle, mitotic (R-HSA-69278)
Hallmark G2M checkpoint (M5901)
Hallmark E2F targets (M5925)
APC/C degradation of cell cycle prot. (R-HSA-174143)
0 10 20 30 40
-Log(q-value)

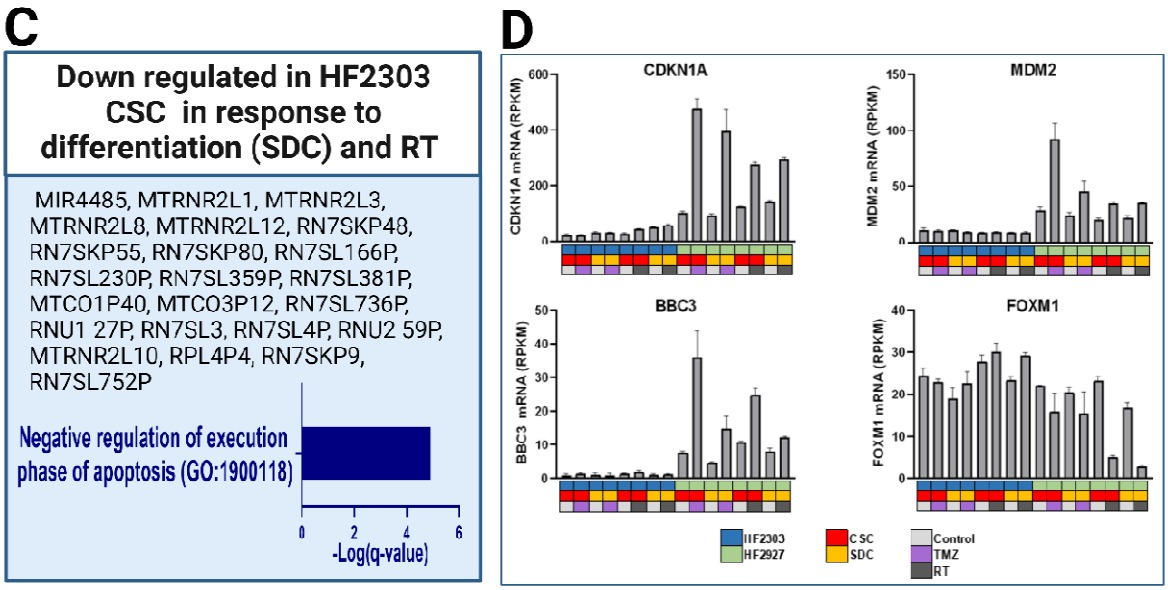

Figure 8: Transcriptional response to genotoxic treatment in glioblastoma cells. Differentially expressed genes between treated and control samples were determined and enrichment performed as described for Fig. 7. **A)** Transcriptional changes in CSCs and SDCs in response to 4-day TMZ treatment (IC40 concentrations). **B)** Transcriptional changes in CSCs and SDCs measured 5 days after one dose radiation (4 Gy). **C)** RNA commonly downregulated in HF2303 CSCs in response to differentiation and RT treatment. **D)** mRNA expression (RPKM) of p53 transcriptional targets CDKN1A (p21), MDM2, and BBC3, and of cell cycle regulators in HF2303 and HF2927 control and treated cells, mean and SE of n=3. Figures created with Biorender.com.

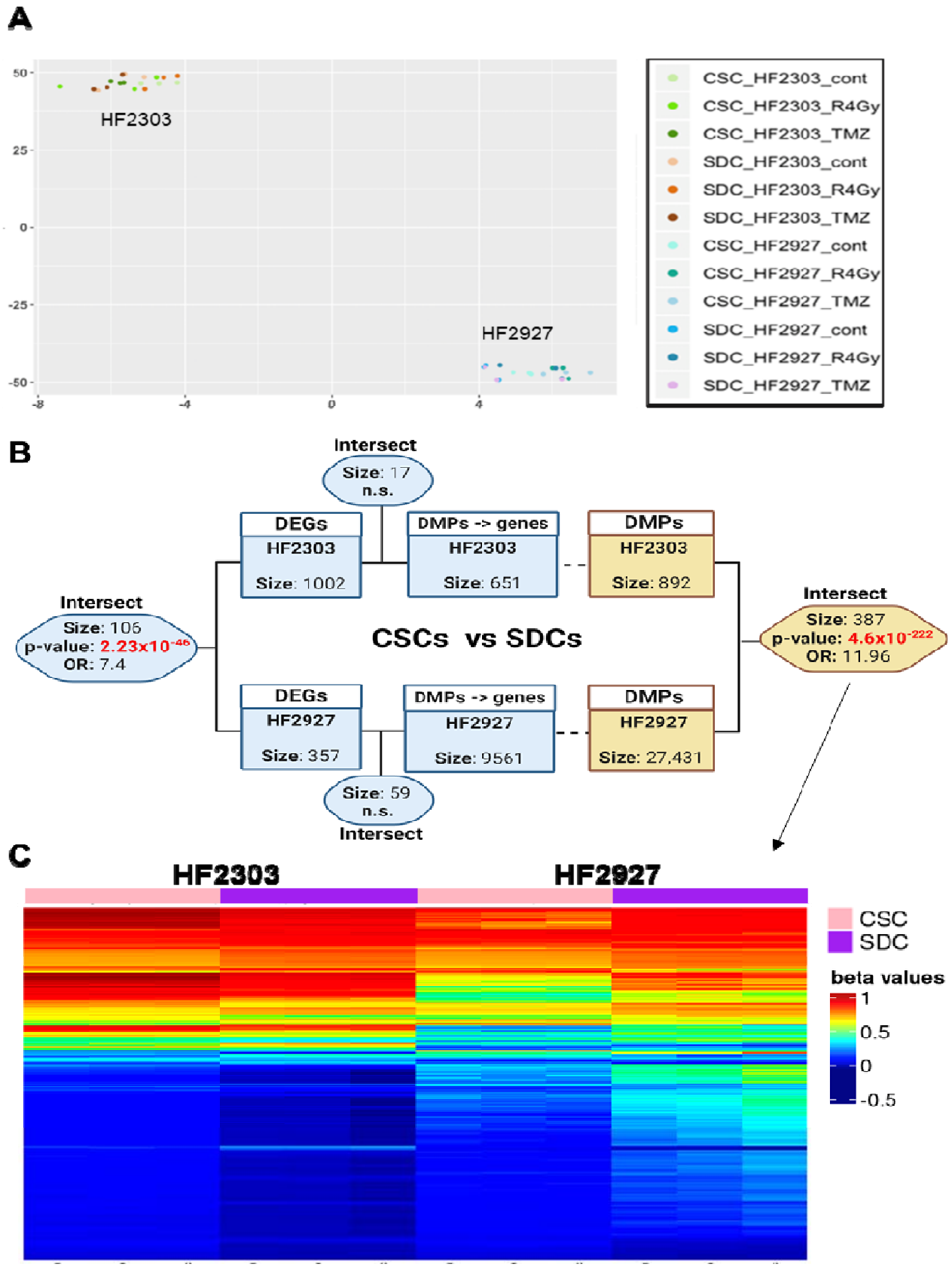
A
HF2303
HF2927
CSC_HF2303_cont
CSC_HF2303_R4Gy
CSC_HF2303_TMZ
SDC_HF2303_cont
SDC_HF2303_R4Gy
SDC_HF2303_TMZ
CSC_HF2927_cont
CSC_HF2927_R4Gy
CSC_HF2927_TMZ
SDC_HF2927_cont
SDC_HF2927_R4Gy
SDC_HF2927_TMZ
B
Intersect
Size: 17
n.s.
DEGs
HF2303
Size: 1002
DMPs -> genes
HF2303
Size: 651
DMPs
HF2303
Size: 892
Intersect
Size: 105
p-value: 2.23x10-46
OR: 7.4
CSCs vs SDCs
Intersect
Size: 387
p-value: 4.6x10-222
OR: 11.96
DEGs
HF2927
Size: 357
DMPs -> genes
HF2927
Size: 9561
DMPs
HF2927
Size: 27,431
Size: 59
n.s.
Intersect
C
HF2303
HF2927
CSC
SDC
beta values
1
0.5
0
-0.5

Figure 9. Genome-wide DNA methylation profiling groups samples by patient of origin and identifies DNA methylation alteration patterns between glioblastoma CSCs and their differentiated progeny. A) t-SNE plot from b-values for all CpG sites comparing HF2303 and HF2927 CSCs and SDCs treated with control, RT or TMZ, in triplicates. **B)** Schematic showing the significant intersect for HF2303 and HF2927 of differentially expressed genes (DEGs) and differentially methylated probes (DMPs) between CSCs and SDCs. The intersect between DMPs annotated to genes (see Methods) and DEGs are shown. Significance of the intersections was determined using GeneOverlap, p-values and estimated odds ratio are shown; n.s., nonsignificant. **C)** Heatmap showing the β-values for the 387 DMPs common to HF2303 and HF2927. Figure 9B created with Biorender.com.